universität wien

MASTERARBEIT / MASTER'S THESIS

Titel der Masterarbeit / Title of the Master's Thesis

„Magnetic Nanogels“

verfasst von / submitted by

Ivan Novikau

angestrebter akademischer Grad / in partial fulfilment of the requirements for the degree of

Master of Science (MSc)

Wien, 2020 / Vienna, 2020

Studienkennzahl lt. Studienblatt / degree programme code as it appears on the student record sheet:	UA 066 910
Studienrichtung lt. Studienblatt / degree programme as it appears on the student record sheet:	Masterstudium Computational Science
Betreut von / Supervisor:	Assoz. Prof. Dr. Sofia S. Kantorovich, Privatdoz.

Abstract

Magnetic nanogels represent a cutting edge of magnetic soft matter research due to their numerous potential applications. Here, using Langevin dynamics simulations, was analysed the influence of magnetic nanogel concentration and embedded magnetic particle interactions on the self-assembly of magnetic nanogels at zero field. For this, was calculated radial distribution functions and structure factors for nanogels and magnetic particles within them. Was found that, in comparison to suspensions of free magnetic nanoparticles, where the self-assembly is already observed if the interparticle interaction strength exceeds the thermal fluctuations by approximately a factor of three, self-assembly of magnetic nanogels only takes place by increasing such ratio above six. This magnetic nanogel self-assembly is realised by means of favourable close contacts between magnetic nanoparticles from different nanogels. It turns out that for high values of interparticle interactions, corresponding to the formation of internal rings in isolated nanogels, in their suspensions larger magnetic particle clusters with lower elastic penalty can be formed by involving different nanogels. Finally, was shown that when the self-assembly of these nanogels takes place, it has a drastic effect on the structural properties even if the volume fraction of magnetic nanoparticles is low.

Zusammenfassung

Magnetische Nanogele stellen aufgrund ihrer zahlreichen Anwendungsmöglichkeiten eine sehr perspektivische Richtung für die Erforschung magnetischer weicher Materie dar. Hier wurde mithilfe von Langevin-Dynamiksimulationen der Einfluss der magnetischen Nanogelkonzentration und der Wechselwirkungen eingebetteter magnetischer Partikel auf die Selbstorganisation magnetischer Nanogele im Nullfeld analysiert. Hierzu wurden radiale Verteilungsfunktionen und Strukturfaktoren für Nanogele und darin enthaltene magnetische Partikel berechnet. Es wurde festgestellt, dass im Vergleich zu Suspensionen freier magnetischer Nanopartikel, bei denen die Selbstorganisation bereits beobachtet wird, wenn die Wechselwirkungsstärke zwischen den Partikeln die thermischen Schwankungen um etwa den Faktor drei übersteigt, die Selbstorganisation magnetischer Nanogele nur durch Erhöhen dieses Verhältnisses über sechs erfolgt. Diese magnetische Selbstorganisation der Nanogele wird durch günstige enge Kontakte zwischen magnetischen Nanopartikeln aus verschiedenen Nanogelen realisiert. Es zeigt sich, dass für hohe Werte von Interpartikelwechselwirkungen, die der Bildung von Innenringen in isolierten Nanogelen entsprechen, in ihren Suspensionen größere magnetische Partikelcluster mit geringerer elastischer Strafe durch Einbeziehung verschiedener Nanogele gebildet werden können. Schließlich wurde gezeigt, dass die Selbstorganisation dieser Nanogele einen drastischen Einfluss auf die Struktureigenschaften hat, selbst wenn der Volumenanteil magnetischer Nanopartikel gering ist.

Contents

[1] this and the following subsection are based on the official documentation taken from the ESPResSo website (http://espressomd.org/html/doc4.1.3/index.html) as of August 2020

[2] a brief description of the P^3M algorithm for dipolar interactions proposed in the work of Juan J. Cerdà et al. [9]

Acknowledgments

I want to thank my scientific advisor for the freedom granted, which was in harmony with constant support. As well, I am extremely grateful to Dr. Elena Minina and Dr. Pedro Sánchez for their help, attention and patience. Furthermore, I would not have done this without the moral and financial support from my family.

Dedicated to S.

Preface

This thesis comprises the material published in 1 peer-reviewed journal article. The emphasis was placed on a brief discussion of the current state of research in the field of magnetic nanogels and a description of the methods used in this study. The article can be found and accessed following the citation below:

- I.S. Novikau, E.S. Minina, P.A. Sánchez, S.S. Kantorovich. 'Suspensions of magnetic nanogels at zero field: Equilibrium structural properties', Journal of Magnetism and Magnetic Materials, Volume 498, (2020).

1 Introduction

Magnetic nanogels have two components: gel and magnetic nanoparticles (MNPs). Their most promising application is the delivery of drugs for the treatment of various diseases, especially cancer [34, 33, 22]. By applying an external magnetic field, it is possible to direct them to the desired place in the human body and then applying an alternating magnetic field, to force them to release useful medicines.

This chapter consists of three sections which are devoted to nanogels, MNPs and magnetic nanogels (a mixture of nanogels and MNPs).

1.1 Nanogels

This section is devoted to hydrogels because they are the basis of most experimental implementations of magnetic nanogels. According to the definition of the International Union of Pure and Applied Chemistry (IUPAC), the gel as a nonfluid colloidal network or polymer network that is expanded throughout its whole volume by a fluid. And the hydrogel, in particular, is a gel in which the swelling agent is water [46].

Hydrogels can be synthesized from such synthetic polymers as *poly(hydroxyalkyl methacrylate)s, poly(acrylamide)s, poly(vinyl alcohol)s, poly(N-vinyl pyrrolidone)s and poly(acrylic acid)s* [25].

Besides synthetic polymers, hydrogels can be obtained from organic materials: methylcellulose, agarose, elastin-like polypeptides, hyaluronan, and other natural polymers. Thanks to that they can be applied in agriculture [10].

Further in the text when it comes to nanogels, in the most cases hydrogels are meant. But here it is worth noting that a large variety of nanogels, differing both in their composition and structure, was synthesized and studied. For example, core-shell nanogels, Janus nanogels, hollow nanogels, and interpenetrating network (IPN) nanogels [32]. The diameter of nanogels lays within the interval of 10 nm to 10 μm (see Figure 1).

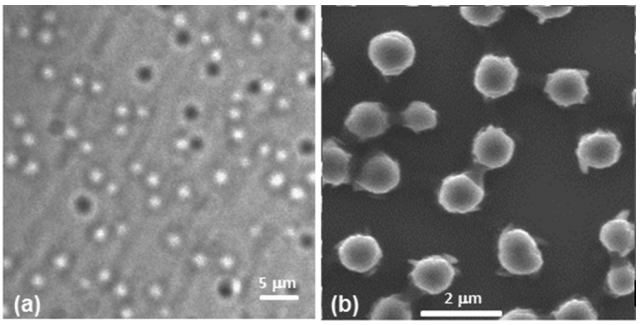

Figure 1: Optical microscopy and scanning electron microscope (SEM) images for various nanogels [49].

1.1.1 Synthesis

When synthesizing nanogels, special attention is usually paid to the control of the distribution of their sizes, their colloidal stability, the distribution of crosslinkers, and other functional groups, for example, magnetic dipoles. In other words, it is important to make nanogels of approximately the same size and to control the level of polymer crosslinking so that the nanogels do not fall apart.

There are three main ways to synthesize nanogels [32]:

1. **From monomer.** By taking vinyl monomers and adding bifunctional cross-linking monomers (for example: *N, N-methylenebisacrylamide* (MBA)).

2. **From polymer.** Polymer solutions can be chemically or physically cross-linked.

3. **From macrogels.** If one takes macrogels and to grind them mechanically, they will be turned into nanogels. But apparently, this is not the most successful method, because it is almost impossible to control the shape and size of the nanogels.

Even if we discard the third method, the first two ones already offer a huge variety of combinations of basic reagents. Moreover, there are at least three types of approaches for nanogels formation:

1. **Homogeneous nucleation.** A solution of soluble monomer and cross-linking agent are fed into the reactor and nanogel particles are formed by means of polymerization. The polymer must be insoluble under the polymerization conditions, otherwise, nanogels will form macrogel. *Poly(N-isopropylacrylamide)* (or PNIPAM) nanogels could be obtain in such way if monomers will be polymerized in water at 70°C (see Figure 2).

   With this approach, there are three options for polymerization: nanogel formation from dilute polymer solution, emulsion polymerization, and surfactant-free emulsion polymerization.

2. **Nanogels from Emulsification.** With this approach, a water-in-oil pregel emulsion is created in oil or brine phase. The term pregel usually means either a solution of polymers or monomers. And then this emulsion of droplets undergoes a chemical reaction to gel their content (see Figure 3).

3. **Nanogels by Polymer Complexation.** In this case, the main idea is to mix diluted solutions of oppositely charged polyelectrolytes to gain colloidally dispersed, polyelectrolyte complexes.

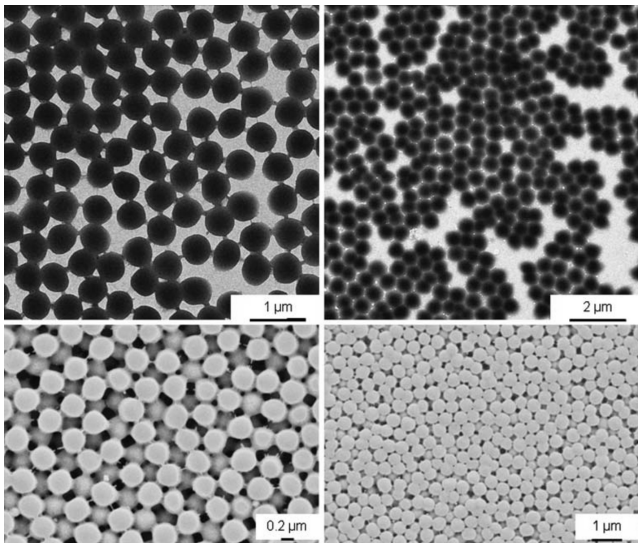

Figure 2: Electron microscopy images of PNIPA-xl-A (left hand) and PNIPAM-xl-C (right hand) after ultrafiltration and redispergation; TEM (upper row) and SEM images (lower row) [48].

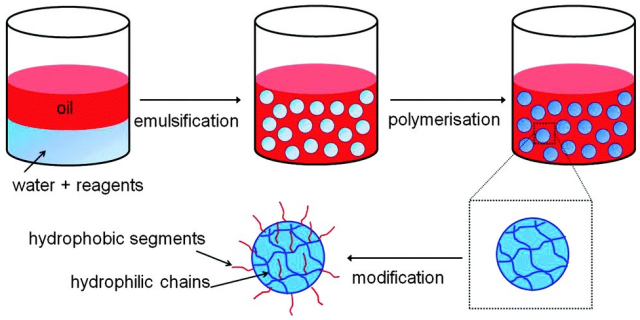

Figure 3: Schematic illustration of the most common approach to amphiphilic microgel production via emulsion templating and post-modification of the microgel. The hydrophobic and hydrophilic moieties are colored in red and blue, respectively [24].

1.1.2 Theory

The theoretical description of nanogels is based on more than a century of experience in polymer research [**ChemistryUSA.pdf**].

There are several theoretical models of nanogel swelling [42, 41]. Understanding the physics of this process is very important for drug delivery problem [33].

There are also theories describing the dynamics of nanogels, which are consistent with the experimental results [38].

1.2 Magnetic nanoparticles

Magnetic nanoparticles (MNPs), in particular, their stable suspensions in magnetopassive carriers (ferrofluids), have been studied since the 60s of the 20th century. They have found their use in medicine for drug targeting, contrast agents, hypothermia cancer-treatment therapy, cell manipulation, sensors, and others [6]; they also improved various technologies, such as loudspeakers(efficient cooling), seals(USP 3,620,584), purifications, dampers, and separation devices. Such diverse applications are made possible by functionalizing the nanoparticle surfaces, tuning their shape and controlling their internal crystalline structure [45].

MNPs can be divided depending on their size into three types: multidomain, single domain, and superparamagnetic [23]. To characterize particles, it is convenient to use their coercivity (see Figure 4). What measures how ferromagnetic material can withstand an external magnetic field without becoming demagnetized. With a decrease in the size of single-domain nanoparticles, the role of the Neel mechanism of relaxation of the dipole moment increases. For multidomain nanoparticles, respectively, the Brownian mechanism of relaxation of the dipole moment plays the key role.

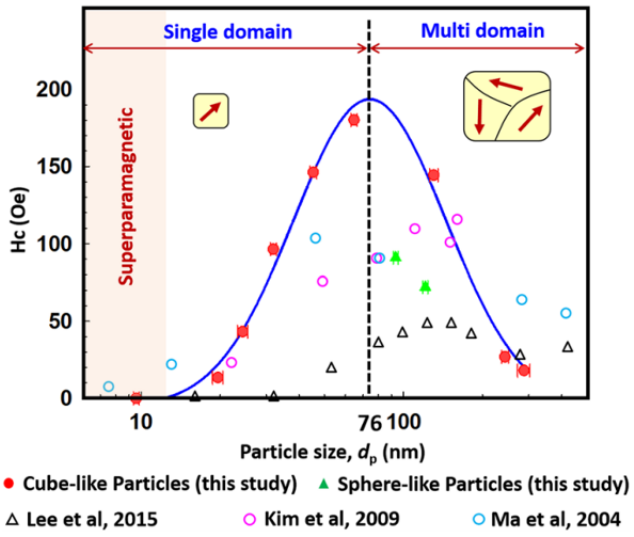

Figure 4: Magnetic performance of Fe3O4 nanoparticles measured at 300K: particle size dependence of the coercivity (**Hc**).

The materials of which MNPs consist can be divided into four groups: ferromagnetic, ferrimagnetic, antiferromagnetic, and paramagnetic [47]. The dif-

ferences between the materials of different groups is the mutual orientation of the dipole moments between the domains (see Figure 5).

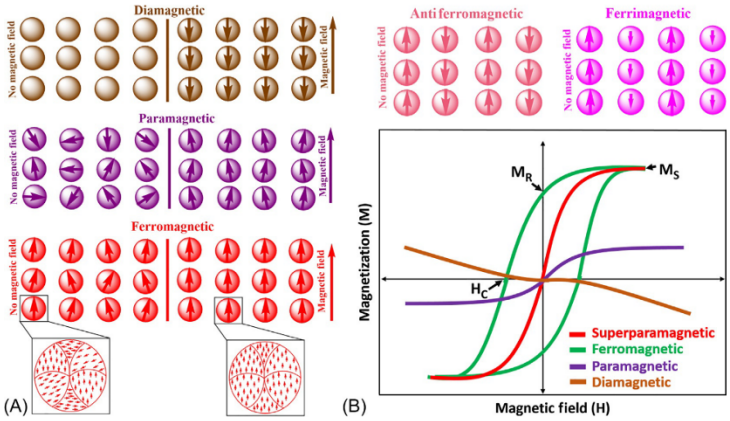

Figure 5: (A) Schematic illustration of the arrangement of the magnetic dipoles of various types of magnetic materials (diamagnetic, paramagnetic, ferromagnetic, antiferromagnetic, and ferrimagnetic), and their response in the absence and in the presence of an external magnetic field. (B) Representative hysteresis loops that illustrate the magnetic behaviour of materials when an external field is applied ($\mathbf{H_c}$, coercive field; $\mathbf{M_r}$, remanent magnetization; $\mathbf{M_s}$, saturation magnetization) [47].

Sizes of single domain MNPs lay in the range of 10-100 nm depending on the material (see Figure 6).

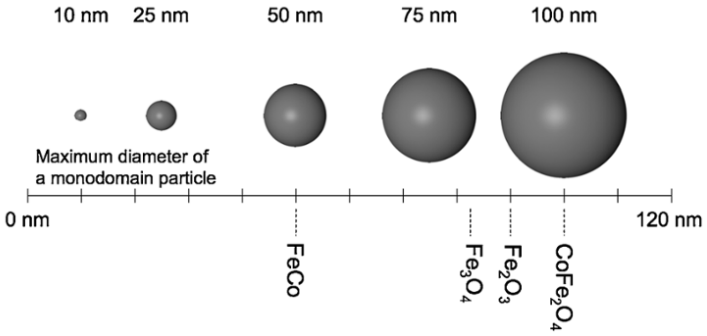

Figure 6: Frontier magnetic nanoparticle(MNP) size between multidomain and monodomain MNPs depending on their crystalline structure [6].

1.2.1 Dipole-dipole interaction and response to an external magnetic field

Regarding the MNPs, for simplicity they are introduced by assigning a permanent magnetic moment: a point dipole, $\vec{\mu}$, placed in their centres, which could freely rotate in three-dimensional space. Thus, the interaction between magnetic particles can be reduced to a dipole-dipole interaction, which can be described by the following potential:

$$U_{dd}\left(\vec{r}_{ij}\right) = \frac{\left(\vec{\mu}_i \cdot \vec{\mu}_j\right)}{r^3} - \frac{3\left(\vec{\mu}_i \cdot \vec{r}_{ij}\right)\left(\vec{\mu}_j \cdot \vec{r}_{ij}\right)}{r^5}, \tag{1}$$

where $\vec{\mu}_i$, $\vec{\mu}_j$ are the respective dipole moments of the interacting particles and $\vec{r}_{ij}$ is the vector between their centres, μ_0 is permeability of vacuum, or magnetic constant.

It is worth noting that the magnetic field of a magnetic dipole is equal up to a factor to the electric field of an electric dipole, if in the expression for the latter, the electric dipole moment is replaced by the magnetic dipole moment. And to obtain the field created by an electric dipole, it is necessary to use the expansion in a Taylor series, as a result of which a nonzero, so-called, dipole term or dipole moment appears in the potential created by a point dipole, which dominates over the quadrupole, octupole, and other, even faster decaying terms [36, Chapter 10]. By their nature, the forces of magnetic interaction are much weaker than electrostatic forces. And the dipole moment is weaker than the monopole moment. Thus, the dipole magnetic interaction is sufficiently weak and safe for living beings, but at the same time, these forces are quite enough for the implementation of drug delivery techniques.

It is convenient to determine the strength of the dipolar interaction between two identical MNPs via the dipolar coupling parameter λ, which is the ratio of the minimum energy of two particles in the head-to-tail configuration to their thermal energy. Defined by the following expression:

$$\lambda = \frac{\mu_0 \vec{\mu}^2}{4\pi\sigma^3 k_{\mathrm{B}} T}, \tag{2}$$

where σ denotes the diameter of the particle, $|\vec{\mu}|$ is the magnitude of the magnetic moment, and $k_{\mathrm{B}}T$ is the thermal energy. Normally λ ranges from below one to eight for single domain particles. For large λ MNPs form clusters, while for small λ a system of MNPs is spatially uniform. It is also worth noting that the magnetic moment of the particles $|\vec{\mu}|$ scales like the third power of the core diameter.

In molecular dynamics simulations, MNPs are usually treated as soft spheres. The interaction between them is described using Weeks–Chandler–Andersen (WCA) potential [51]. This is a repulsive potential that prevents the MNPs' from sticking together into one lump.

Under exposure of external magnetic field takes place the particle field in-

teraction:

$$U_{\text{Zeeman}} = -\vec{\mu} \cdot \vec{H}, \tag{3}$$

where $\vec{H}$ is the external magnetic field and $\vec{\mu}$ is the magnetic moment of a given particle.

The ratio of the minimum of Zeeman energy per particle to the thermal one is called the Langevin parameter

$$\alpha = \frac{\mu_0 \vec{\mu} \vec{H}}{k_{\text{B}} T}. \tag{4}$$

Without an external field applied, the magnetic moments of the particles are randomly aligned, and their sum is zero. In the field the magnetic moments tend to align parallel to it, that leads to a significantly enhanced magnetization of the system.

The magnetization of a system of non-interacting dipoles can be approximated using the Langevin parameter α [50]

$$\vec{M}(\alpha) = \vec{M}_s L(\alpha), \tag{5}$$

where $\vec{M}_s$ is the saturation magnetization given by the sum of all magnetic moments $\vec{\mu}$ in the system normalized by volume V:

$$\vec{M}_s = \frac{1}{V} \sum_i \vec{\mu}_i. \tag{6}$$

$L(\alpha) = \left(\coth \alpha - \frac{1}{\alpha}\right)$ is called the Langevin function. If magnetic particles are influenced by the field created by the surrounding particles, then the magnetization generally is increased, in particular for intermediate external fields. In this case, the first order mean-field approach is used [50]

$$\vec{M}_1(\alpha) = \vec{M}_s L(\alpha + cL(\alpha)), \tag{7}$$

where c depends on the density of magnetic particles and the system's dimension (monolayer or bulk).

In computer simulation of the system with the two potentials mentioned above (WCA and dipole-dipole interaction) the dipoles assemble into chains (see Figure 7). The figure shows what kind of chains are formed, but their length and shape strongly depend on the strength of the applied field and the parameters of the dipoles.

This alignment appears in the parallel direction to the magnetic field to keep the energetically more favorable state. This

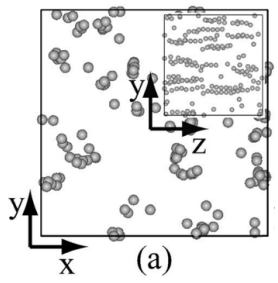

Figure 7: Snapshots of the dipolar hard-sphere systems in chains fluid phase [20]

phase state is characteristic of dipolar fluids, or ferrofluids.

The combination of nanoparticles in chains further enhances the magnetic response of the system, which leads to a higher initial susceptibility. It is given by the slope of the magnetization curve in the zero-field limit

$$\chi = \frac{\partial \vec{M}(\vec{H})}{\partial \vec{H}}. \tag{8}$$

It is shown that chains form more complex structures (see Figure 8). There is also a theoretical model that describes the physics of ferrofluids, staying in good agreement with the results of computer simulation [45].

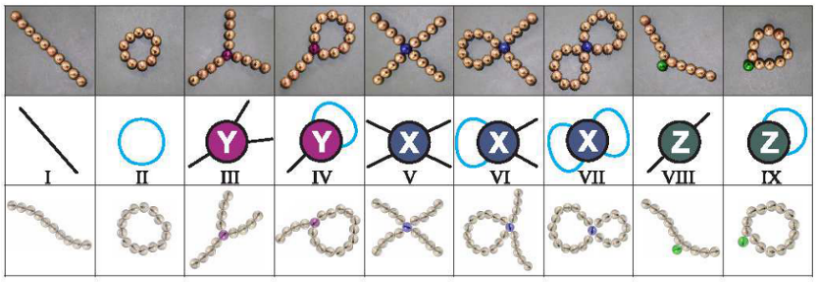

Figure 8: Top row: photographs of commercially available magnetic beads; middle row: topological classification used in the proposed theoretical approach; bottom row: structures extracted from Monte Carlo computer simulations analyzed in this manuscript [45].

1.3 Magnetic nanogels

Magnetic nanogels (MNGs) are MNPs enclosed in ordinary nanogels. The first scientific article devoted to this topic was published in 2000 (according to Google Scholar, to be precise it is dedicated to microgels) [13].

Their properties could be dynamically changed depending on an applied magnetic field [15]. Also they preserve features of ordinary polymer gels, which can be manipulated by changing pH, temperature, light intensity, applied electric field and composition of the medium in which they are located. Thus, MNGs are unique in their own way and called smart materials.

The external magnetic field is able to change the structure of the colloid consisting of nanogels from anisotropic to isotropic and vice-versa (see Figure 9). This makes it possible to study the influence of an external magnetic field on the elastic moduli.

Another important property of MNGs is that the external magnetic field change their shape, due to the presence of MNPs inside them (see Figure 10).

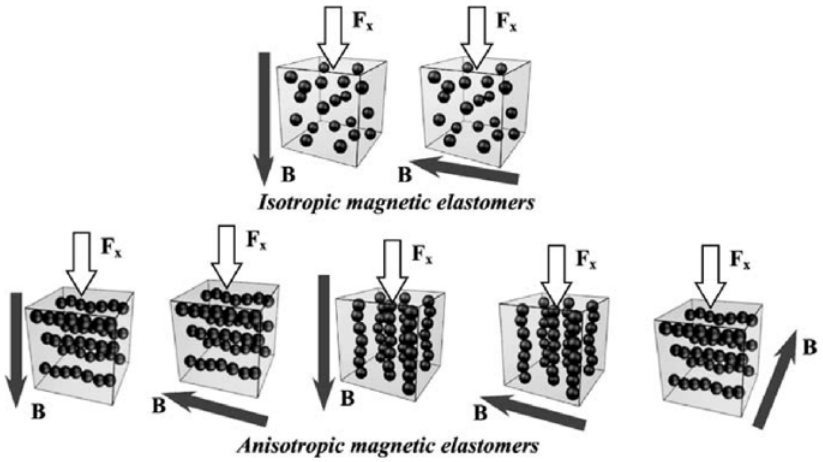

Figure 9: Experimental possibilities in the study of the influence of external magnetic field on the elastic modulus. White arrows indicate the direction of the force; black arrows show the direction of the magnetic field [15].

On this effect is the drug delivery based. If an alternating magnetic field of a certain frequency will be applied, then the particles of the drug will start to be released from the MNG to the outside.

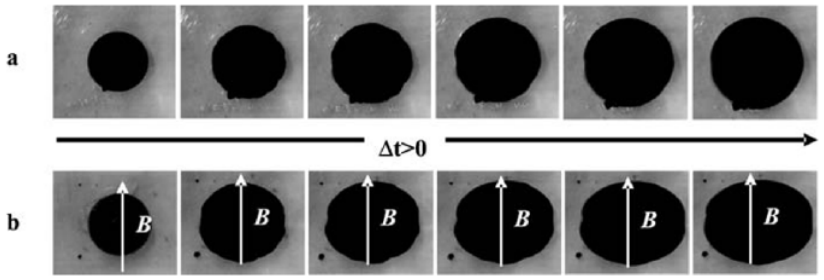

Figure 10: Swelling kinetics of (a) iron- and (b) magnetite-loaded mPDMS spheres. The arrow shows the direction of the applied magnetic field during preparation [15].

1.3.1 Architecture

It is convenient to divide the architecture of hybrid nanogels into two classes (see Figure 11) according to how the nanoparticles are attached to the polymer network [18]: materials that show weak physical interactions such as van der Waals forces, weak electrostatic interactions, or hydrogen bonding (Class 1); and materials show permanent strong physical or chemical interactions between

the two species(monomers and nanoparticles) such as covalent bonding or strong electrostatic interactions, strong hydrogen bonding or strong coordinative bonds (Class 2);

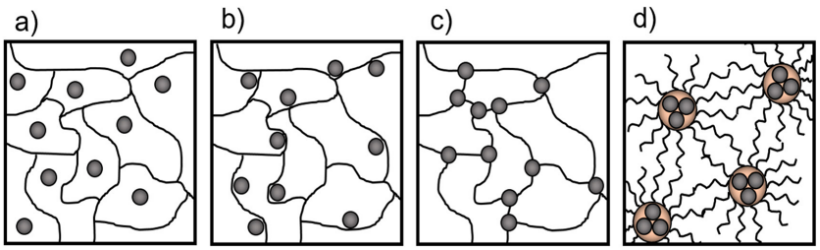

Figure 11: Schematic drawing of different polymer gel frameworks with incorporated nanoparticles; (a) chemically cross-linked polymer network with entrapped particles, (b) chemically cross-linked polymer network with physical interactions between polymer and embedded particles (Class 1 type), (c) particle cross-linked hybrid network (chemical interactions, Class 2 type) and (d) magnetic particle loaded bridged micelles [50]

Most studies are devoted to magnetic nanogels of Class 1. While magnetic nanogels of Class 2 [4, 7, 27, 40, 39] are less likely to lose MNPs that might be toxic or their loss might lead to the reduction of the controllability. The stability of the polymer network is also higher for Class 2. The advantage of the Class 1 architecture may be that the magnetic particles are more mobile in the nanogel, which can be used, for example, for effective internal magnetic heating.

1.3.2 Synthesis

The approaches described in the literature on the synthesis of magnetic nanogels can be divided into two groups (see Figure 12): particle-first and polymer-first.

The idea of a polymer-first approach is to synthesize a polymeric network, and then embed MNPs into it. For example, it is possible to make the nanogel swell in the presence of ferrofluid [30] or to synthesize MNPs using a nano-gel as a framework [55]. Another option is loading an already existing nanogel with magnetic cobalt ferrite ($CoFe_2O_4$) particles exploiting electrostatic interactions between the polymer matrix and the particles by vortex this mixture [2]. A strength of the polymer-first approach is that the previously prepared polymer network can be synthesized in a controlled way independently from magnetic nanoparticles. However, the following *in situ* synthesis of magnetic particles is partly limited.

In turn, the particle-first approach is based on fact that the particles are first synthesized, and only then the polymer network around them is arranged. This is possible due to polymerization in the presence of MNPs [43]. The advantage of this method is that MNPs can be synthesized without restrictions from the side of nanogels, and their size distribution can be controlled.

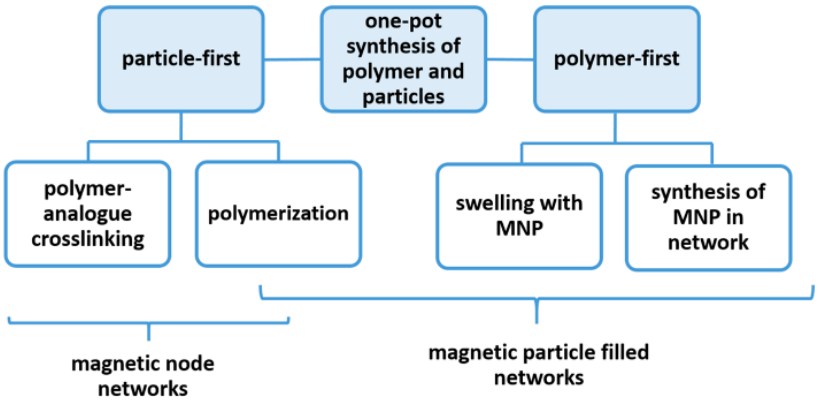

Figure 12: Schematic drawing of different synthesis strategies towards magnetic polymer gels. One can distinguish between the simultaneous one-pot synthesis of the polymer and the magnetic particles, or the polymer- or particle-first method with subsequent synthesis of the other component. Only the particle-first method with polymer-analogue cross-linking results in magnetic node networks, all other methods result in magnetic particle filled networks [50].

1.3.3 Theory

There are several known attempts to theoretically describe the physics of magnetic nanogels with varying degrees of success. However, due to the relative complexity of the magnetic nanogels themselves, it is very difficult to present all the details in the form of a simple theoretical model.

The first class of theoretical models is based on sewing MNPs into a network of springs (see Figure 13) [35, 21]. The main problem of this approach is the impossibility of applying non-affine (see Figure 14) transformations to the studied structure.

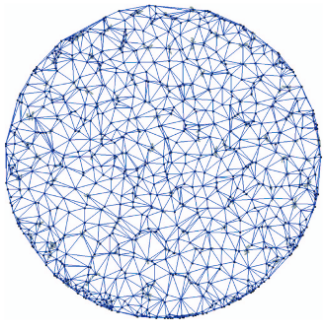

Figure 13: Two-dimensional slice of a three-dimensional cylinder, nanoparticles in the nodes, based on real experimental data [35].

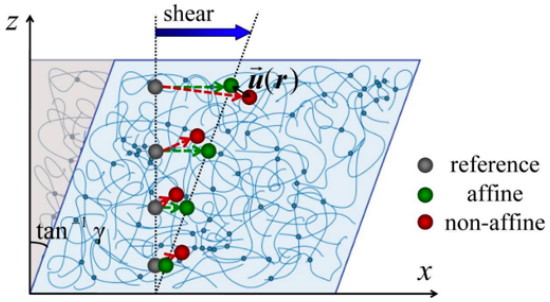

Figure 14: Illustration of affine and non-affine shear deformation of polymer gels with entrapped tracer beads. The non-affine deviation, $\vec{u}$ is defined as the difference between the real displacement and affine dis-placement of a tracer bead [53]. This figure is adopted from [5].

In the second class of models, nanogel and immersed MNPs are described as a homogeneous elastic continuum with linear magnetization [26, 56]. The disadvantage of this model is that it does not take into account the individual MNPs inside nanogel and all the associated effects, although in principle it is able to describe a gel with large microparticles inside. The strength is that can be solved analytically.

There are models based on the calculation of the matrix-mediated interactions between individual magnetic particles [56] and classical density functional [11].

1.4 Summary

Nanogels prepared from vinyl monomers with some form of free radical polymerization are most often found in the scientific literature. The most common methods of polymerization are conventional and surfactant-free emulsion polymerizations, the first one being more common in commercial samples, and the second more convenient for laboratory research. It is also noteworthy that all polymerization schemes described above are successfully used to create latex and other polymers.

MNPs are well studied experimentally and theoretically, there are many approaches to their synthesis, and there are examples of successful commercial applications.

Magnetic nanogels are relatively young, the first description in the scientific literature occurs less than 20 years ago. But there are already many recipes to their synthesis, several theoretical models and many articles devoted to their potential use in the field of drug delivery.

To the best of my knowledge, no theoretical study on magnetic nanogel suspensions is yet available in literature. It seems interesting to investigate how the density of a suspension of magnetic nanogels and interaction strength between MNPs inside them will affect their structural properties. And also,

how will it impact the diffusion of a single nanogel? For these purposes, the molecular dynamics simulation method will be used, since it allows us to study the largest range of effects, more than any other analytical approach existing today.

2 Model and Methods

The next step is to search for a simple coarse-grained (see Figure 15) computer simulation model that adequately represents the magnetic nanogel mentioned in the first chapter.

As it has been said in the conclusion of the previous chapter, the main method to be used in this work is Molecular Dynamics Simulations (MD). Therefore, below will be discussed the implementation of a numerical model of a magnetic nanogel within the framework of the MD method. In addition, the chapter describes the approaches to the analysis of data obtained in simulations, which allow comparing simulations with real experimental results.

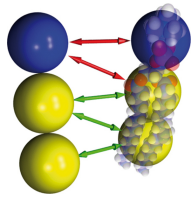

Figure 15: Example of coarse-grained model of a lipid
The picture is taken from espressomd.org (CC BY-SA https://creativecommons.org/licenses/by-sa/3.0)

2.1 Model

A year earlier an appropriate model was developed [28] in the same research group where the current study was carried out.

The magnetic nanogel model is based on a bead-spring representation of the polymer chains and the embedded magnetic particles. Briefly, the setup of each nanogel particle is performed in the following way. First, polymer precursors are modelled as chains of spherical beads with unit dimensionless mass and diameter. They have a steric repulsion given by a truncated and shifted Lennard-Jones potential, or Weeks-Chandler-Andersen (WCA) potential [51]:

$$U_{WCA}(r) = \begin{cases} 4\left[r^{-12} - r^{-6}\right] + 1, & r \leqslant 2^{1/6} \\ 0, & r > 2^{1/6} \end{cases}, \tag{9}$$

where r is the centre-to-centre distance between the interacting particles. Here, the depth of the Lennard-Jones potential well was set to unity, thus introducing a scaling for all energies in the simulation protocol. These beads form the polymer chain backbones by means of finitely extensible nonlinear elastic (FENE) springs connected to their centres:

$$U_{FENE}(r) = -\frac{1}{2}\epsilon_f r_f^2 \ln\left[1 - \left(\frac{r}{r_f}\right)^2\right], \tag{10}$$

where $\epsilon_f = 22.5$ is the dimensionless interaction strength and $r_f = 1.5$ is the maximum bond extension. Nanogel particles are obtained by equilibrating $N_p = 6$ polymer chains with $L = 100$ beads each inside a spherical confinement wall with volume fraction of approximately $\phi_p \approx 0.1$. After equilibration, interchain crosslinks are randomly introduced according to a minimum interparticle distance criterium, up to reach a fraction of crosslinks of $\phi_{\text{links}} = 0.17$. Each crosslink consists in a elastic spring connecting the centres of the newly bonded

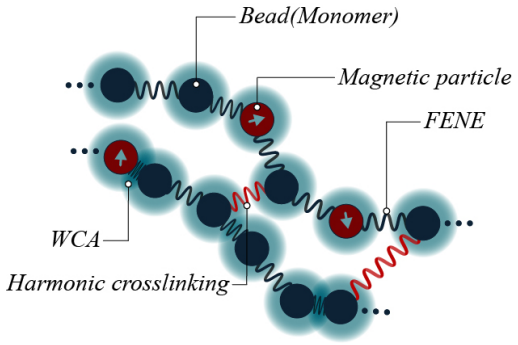

Figure 16: Bead-spring representation of the internal structure of a model magnetic nanogel. Arrows inside particles indicate the presence of a point magnetic dipole.

pair of particles. In order to speed up the crosslinking process, harmonic springs are used for this purpose:

$$U_h(r) = -\frac{1}{2}Kr^2. \tag{11}$$

By using $K = 10$, was ensured that the mechanical effect of these springs is equivalent to the FENE bonds connecting the precursor backbones. For further details on the crosslinking protocol see Reference [29]. Regarding the magnetic particles, for simplicity they are introduced by assigning a permanent magnetic dipole, $\vec{\mu}$, at the centre of randomly selected beads, up to a fraction of $\phi_{\mathrm{m}} = 0.1$. Therefore, these magnetic beads interact by means of the dipole-dipole pair potential (see Equation 1). These long-range magnetic interactions were calculated using the dipolar $\mathrm{P^3M}$ algorithm, which will be discussed below. Figure 16 shows a sketch of this bead-spring representation of our model magnetic nanogel particles.

The main disadvantage of this model is that it is a coarse-grained model: several subunits of a polymer are represented by a single bead. At the same time, this is the most important advantage of this model. Its simplicity allows to make simulations in a reasonable time, not only of a suspension of magnetic nanogels, but also put it under external magnetic field and in the channel with a flow. Such an investigation today would be overly expensive, if at all possible, for the atomistic model. Also, the randomness of cross-linking and dipole allocation makes the model more similar to real magnetic nanogels.

2.2 Molecular dynamics

This method models the behavior of particles (molecules or nanoparticles) in the inter-atomic potential or molecular force field created by other particles. To calculate the trajectory of motion of an individual particle at each step of integration, it is necessary to solve the system of equations of Newtonian

mechanics without considering quantum effects. This is the responsibility of the so-called integrator, which underlies each MD algorithm. MD has been actively developing for more than half a century (see Figure 17). With the right choice of interaction potentials and good numeral integrator, the results obtained can be very close to the experimental data [19].

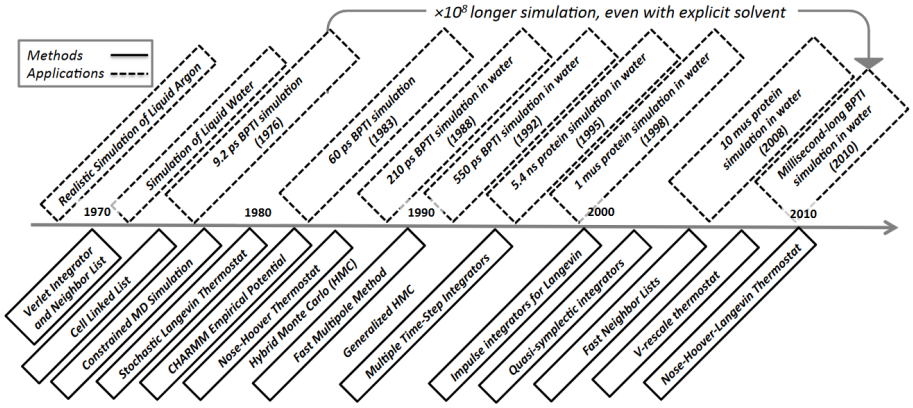

Figure 17: A time line of selected developments in MD simulation [8].

Suppose that one of the integrators is selected, then the entire MD algorithm is reduced to the following (see Figure 18).

An interesting characteristic of the MD method is the so-called Lyapunov instability. This means that the slightest perturbation of the system radically changes its trajectory. More precisely, the difference between the initial trajectory (if the perturbation had not happened) and the new disturbed trajectory grows exponentially, which leads to the two uncorrelated trajectories.

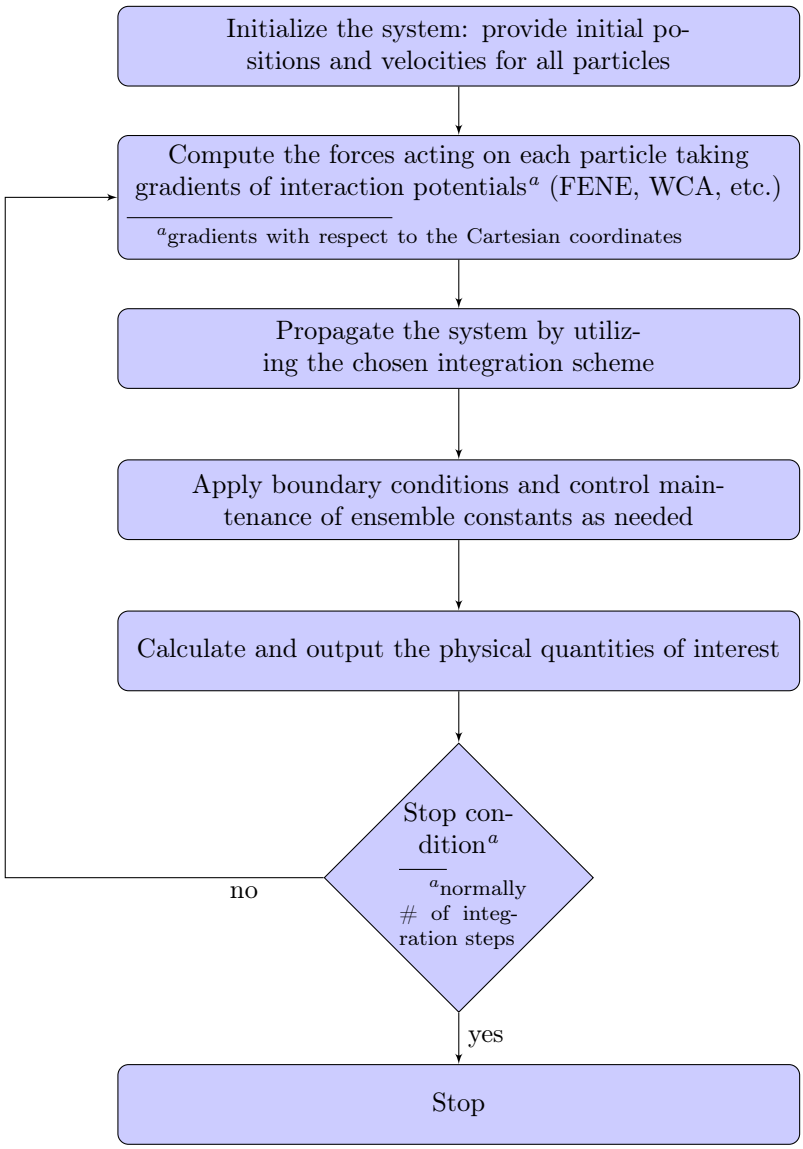

Figure 18: A generalized MD algorithm

2.2.1 ESPResSo

Only taking into account the abundance of varieties of molecular dynamics integrators it is necessary to choose simulation software, where integrator itself and other required algorithms(will be discussed below) for simulations of magnetic nanogels will already be correctly implemented. Moreover, this software must support the ability to parallelize computations. The optimal option was the open-source Extensible Simulation Package for Research on Soft Matter (ESPResSo) (see Figure 19) [52]. Among the advantages are a convenient Python interface over fast "C++ back-end", a lot of manuals and a responsive community of developers who are actively involved in the development of this project.

Figure 19: The logo of ESPResSo has been made using the software itself
The picture is taken from espressomd.org (CC BY-SA https://creativecommons.org/licenses/by-sa/3.0)

2.2.2 Velocity-Verlet[3]

At the moment of time t having position $\boldsymbol{x}_i$, velocity $\boldsymbol{v}_i$ and applied force $\boldsymbol{F}_i\left(\{\boldsymbol{x}_j\}, \boldsymbol{v}_i, t\right)$ for each particle i of a certain mass m_i, one wants to know the position, velocities and forces acting on these particles at the moment of time $t + dt$. The force contains result of interaction of particles with each other and with an external stochastic thermostat, which mimics ambient liquid (water).

ESPResSo utilizes classical one Velocity-Verlet integrator [1], which solves the above problem in four steps:

1. Compute the velocity in a half of time step:

$$\boldsymbol{v}(t + dt/2) = \boldsymbol{v}(t) + \frac{\boldsymbol{F}(\boldsymbol{x}(t), \boldsymbol{v}(t - dt/2), t)}{m} dt/2 \tag{12}$$

2. Compute the new position:

$$\boldsymbol{x}(t + dt) = \boldsymbol{x}(t) + \boldsymbol{v}(t + dt/2)dt \tag{13}$$

3. Compute the force at the new position:

$$\boldsymbol{F} = \boldsymbol{F}(\boldsymbol{x}(t + dt), \boldsymbol{v}(t + dt/2), t + dt) \tag{14}$$

4. Compute the new velocity:

$$\boldsymbol{v}(t + dt) = \boldsymbol{v}(t + dt/2) + \frac{\boldsymbol{F}(\boldsymbol{x}(t + dt), t + dt)}{m} dt/2 \tag{15}$$

[3]this and the following subsection are based on the official documentation taken from the ESPResSo website (http://espressomd.org/html/doc4.1.3/index.html) as of August 2020

2.2.3 Langevin thermostat

The Langevin thermostat, implemented in ESPResSo, needed for simulation of NVT ensemble. It acts on the nanogels as they would be suspended in water, what induces passive Brownian motion of particles. The thermostat relies on an extension of Newton's motion equation to

$$m_i \dot{\boldsymbol{v}}_i(t) = \boldsymbol{f}_i - \gamma_T \boldsymbol{v}_i(t) + \sqrt{2\gamma_T k_B T}\boldsymbol{\eta}_i(t). \tag{16}$$

Here, γ_T is the translational friction coefficient, $\boldsymbol{f}_i$ is the sum of all deterministic forces acting on particle i from other particles, $\boldsymbol{\eta}$ is a stochastic, "thermal" force and k_B is the Boltzmann constant. The friction term controls dissipation in the environment (water) whereas the random force imitates collisions of the beads with water molecules at temperature T and fulfill

$$< \boldsymbol{\eta}(t) >= 0, \tag{17}$$

$$< \boldsymbol{\eta}_i^{\boldsymbol{\alpha}}(t)\boldsymbol{\eta}_j^{\boldsymbol{\beta}}(t') >= \delta_{\boldsymbol{\alpha\beta}}\delta_{ij}\delta(t-t'); \tag{18}$$

$< \cdot >$ denotes the ensemble average, and $\boldsymbol{\alpha}$, $\boldsymbol{\beta}$ are spatial coordinates.

The last two equations imply a delta-correlated (for particle index, coordinate and moment of time) stationary Gaussian process with zero-mean.

The stochastic process $\boldsymbol{\eta(t)}$ is defined on continuous time domain and has to be discretized by taking its realization $\bar{\boldsymbol{\eta}}$ for each component of all the particle forces. The distribution of $\bar{\boldsymbol{\eta}}$ is also uniform and satisfies

$$< \bar{\boldsymbol{\eta}} >= 0, \tag{19}$$

$$< \bar{\boldsymbol{\eta}}\bar{\boldsymbol{\eta}} >= 1/dt. \tag{20}$$

The thermostat also affects the rotational movement of the particles:

$$\boldsymbol{I}_i\dot{\boldsymbol{\omega}}_i(t) = \boldsymbol{\tau}_i - \gamma_R\boldsymbol{\omega}_i(t) + \sqrt{2\gamma_R k_B T}\boldsymbol{\xi}_i(t), \tag{21}$$

where $\boldsymbol{I}_i$ is the particle inertia tensor, $\boldsymbol{\omega}_i$ is the angular velocity, $\boldsymbol{\tau}_i$ is the torque on particle i due to the existence of all other particles, γ_R is the rotational friction coefficient and $\boldsymbol{\xi}_i$ is the Gaussian random torque. For this case, Equations 17-20 (reformulated under Equation 21) also hold.

2.2.4 Domain decomposition: Cell and Verlet lists

It is possible to divide all interactions between particles into two groups: short-range (WCA, FENE, harmonic bonds) and long-range (dipole-dipole interaction).

In this section, we will talk about how was optimized the calculation of short-range interactions. They all have a common feature, namely some cutoff radius r_c. If the distance between the particles exceeds this radius, then there

cannot be a short-range interaction between them corresponding to the given radius.

If the interactions of each particle pair is calculated without the restrictions described above, such calculations will scale as $O(N^2)$. ESPResSo uses two algorithms to make the problem scale in complexity close to linear. Firstly (Cell list), the entire simulation box is divided into the cells, such that the cell size is larger than the maximum interaction range (maximum cutoff radius). In this case interactions only occur between particles within the same and adjacent cells. Secondly (Verlet list), for each particle, a list of possibly interacting with it neighbors is formed based on Cell list. Verlet list for each particle is constructed in such a way that it consists of all other particles, which are in the range of maximum r_c plus some skin ($r_c + skin = R_c$) (see Figure 20). Skin usage allows to update the constructed lists once in several integration steps.

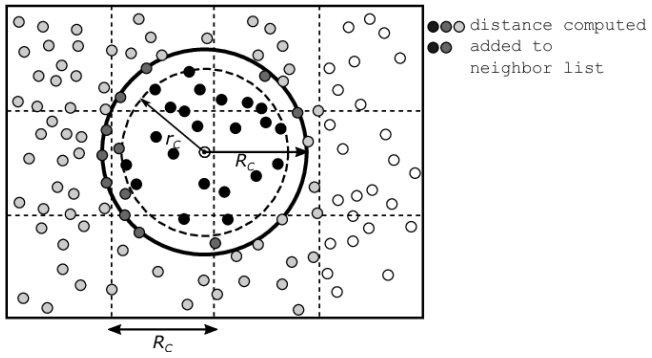

Figure 20: Cell list + Verlet list. The figure is taken from [31].

2.3 Magnetic dipolar interaction

Calculating the energy of dipole-dipole interaction in a system with periodic boundary conditions is not a trivial problem. Since it is necessary to sum up the interaction energy between each pair of magnetic dipoles in boundless space. In general, it is known as calculate potentials in N-body simulation. Fortunately, almost 100 years ago, Paul Peter Ewald came up with an elegant idea for resolving this [14]. Moreover, using the Particle–Particle–Particle–Mesh (P^3M) approach, of which Ewald summation is a part, such problem can be solved in $O(N \log N)$ computational steps.

2.3.1 Ewald summation

The Ewald summation method, as a tool for calculating long-range interactions, is based on dividing the interaction potential (see Equation 1) into two terms, the first describes the short-range interaction, the second represents the long-range; their sums quickly converges in real and in Fourier (reciprocal) spaces,

respectively.

In view of the above, Equation 1 can be represented in an equivalent form[4] as:

$$U_{dd}\left(\vec{r}_{ij}\right) = \left(\boldsymbol{\mu}_i \cdot \nabla_{\boldsymbol{r}_i}\right)\left(\boldsymbol{\mu}_j \cdot \nabla_{\boldsymbol{r}_j}\right)\left(\psi\left(\boldsymbol{r}_{ij}\right) + \phi\left(\boldsymbol{r}_{ij}\right)\right) \equiv v\left(\boldsymbol{r}_{ij}, \boldsymbol{\mu}_i, \boldsymbol{\mu}_j\right), \tag{22}$$

where $\psi\left(\boldsymbol{r}_{ij}\right)$ and $\phi\left(\boldsymbol{r}_{ij}\right)$ are short-distance and long-distance parts of the Coulomb interaction respectively:

$$\psi(\boldsymbol{r}) \equiv \frac{\operatorname{erfc}(\alpha r)}{r}, \tag{23}$$

$$\phi(\boldsymbol{r}) = \frac{\operatorname{erf}(\alpha r)}{r}, \tag{24}$$

their sum is regular at the origin and smooth everywhere. $r = |\boldsymbol{r}|$. Here α is the splitting parameter, which smoothly switches the weights of the potential from real space and the potential from a reciprocal Fourier space in Equation 22.

Such decomposition of the potential underlies in the Ewald formula for the electrostatic energy of a system of dipoles:

$$U = U^{(r)} + U^{(k)} + U^{(\text{self})} + U^{(\text{surf})}. \tag{25}$$

Before proceeding to a more detailed description of this formula, it is interesting to know that it took such form only 41 years after Ewalds original paper, thanks to other works with mathematical refinements of his idea [3].

Consider Equation 25, where $U^{(r)}$ is a real-space energy:

$$U^{(r)} = \frac{1}{2}\sum_{i,j=1}^{N}{}' \sum_{\boldsymbol{n}\in\mathbb{Z}^3} \left(\boldsymbol{\mu}_i \cdot \nabla_{r_i}\right)\left(\boldsymbol{\mu}_j \cdot \nabla_{r_j}\right)\psi\left(\boldsymbol{r}_{ij}\right), \tag{26}$$

the prime over the second sum means that the situation when $i = j$ and $n = 0$ is excluded, i.e. self-interaction is not taken into account.

$U^{(k)}$ in its turn is the reciprocal-space energy is[5]:

$$U^{(k)} = \frac{1}{2V}\sum_{\boldsymbol{k}\neq 0, \boldsymbol{k}\in\mathbb{K}^3} |\hat{\boldsymbol{\rho}}(\boldsymbol{k}) \cdot i\boldsymbol{k}|^2 \breve{\phi}(\boldsymbol{k}), \tag{27}$$

where

$$\hat{\boldsymbol{\rho}}(\boldsymbol{k}) \equiv \mathrm{FT}[\boldsymbol{\rho}](\boldsymbol{k}) = \sum_{i=1}^{N} \boldsymbol{\mu}_i e^{-i\boldsymbol{k}\cdot\boldsymbol{r}_i}, \tag{28}$$

here FT means Fourier transform, and

$$\breve{\phi}(\boldsymbol{k}) = \int \phi(\boldsymbol{r}) e^{-i\boldsymbol{k}\cdot\boldsymbol{r}} d\boldsymbol{r} = \frac{4\pi}{k^2} e^{-k^2/4\alpha^2}. \tag{29}$$

[4] for convenience, the bold characters means vectors

[5] arises from the solution of Poisson equation in reciprocal space [16]

V is the volume of the unit cell ($V = L^3$) and, because of the periodic boundary conditions, wave vectors $\boldsymbol{k} \in \mathbb{K}^3$ are discrete where $\mathbb{K}^3 \equiv \left\{2\pi \boldsymbol{n}/L : \boldsymbol{n} \in \mathbb{Z}^3\right\}$.

This is followed by self-energy $U^{(self)}$ and surface contribution $U^{(surf)}$, which are

$$U^{(\mathrm{self})} = -\frac{2\alpha^3}{3\sqrt{\pi}} \sum_{i=1}^{N} \mu_i^2, \tag{30}$$

$$U^{(\mathrm{surf})} = \frac{2\pi}{(2\epsilon' + 1)\, V} \sum_{i=1}^{N} \sum_{j=1}^{N} \boldsymbol{\mu_i} \cdot \boldsymbol{\mu_j}. \tag{31}$$

ϵ' is the dielectric constant.

If we digress from the dipoles for a minute and set ourselves the task of calculating the energy[6] of the Coulomb interaction of a system of point charges with periodic boundary conditions:

$$E_{\mathrm{Coul}} = \frac{1}{2} \sum_{i,j}^{N} {\sum_{n}}' \frac{q_i q_j}{|\mathbf{r}_{ij} + \mathbf{n}L|}, \tag{32}$$

the sum is poorly convergent. And this is where the stumbling block lies. A step that took decades to overcome. The trick is to add and subtract some conditionally convergent series to the equation above:

$$E_{\mathrm{Coul}} = \sum_{n=1}^{\infty} a_n = \sum_{n=1}^{\infty} (a_n - b_n) + \sum_{n=1}^{\infty} b_n. \tag{33}$$

Let us assume that exist b_n such that the series $\sum_{n=1}^{\infty} (a_n - b_n)$ is absolutely convergent and such that the second series $\sum_{n=1}^{\infty} b_n$ also can be easily computed.

This purely mathematical idea can be elegantly reflected in physics (see Figure 21)!

The next step is to calculate the potential of the new system of charges with assumption that this additional charge distribution surrounding a point charge is a Gaussian $s(\mathbf{r}) = \exp\left(-\alpha^2 r^2\right) \alpha^3/\pi^{3/2}$ [7]. The potential at each point in space has three components: these are point charges (delta functions), their screening charges and smoothly varying background, which compensate the screening. By making simple modifications, replacing point charges with point dipoles[8]. The first two contributions must be counted in real space, and they lead to Equation 26. The third contribution is counted in reciprocal space and leads to Equations 27, 30[9] and 31[10] [3, 16].

Now, knowing the potential energy, one can also get the electrostatic field $\boldsymbol{E}_i = -\nabla_{\boldsymbol{\mu}_i} U$, force $\boldsymbol{F}(\boldsymbol{r}) = \nabla_{\boldsymbol{r}}(\boldsymbol{\mu} \cdot \boldsymbol{E}(\boldsymbol{r}))$ and torque $\boldsymbol{\tau}_i = \boldsymbol{\mu}_i \times \boldsymbol{E}_i$ acting

[6] Gaussian units implied

[7] it is also the origin of Equations 23, 24

[8] replace q_i by $-\boldsymbol{\mu}_i \cdot \nabla_{r_i}$

[9] corrects the spurious "self" interaction included in the Equation 27

[10] case $k = 0$, which is omitted in the Equation 27

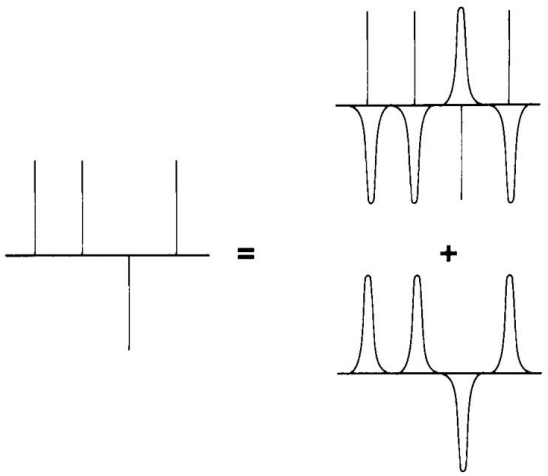

Figure 21: A set of point charges may be considered a set of screened charges minus the smoothly varying screening background [16].

on a single dipole. In this step, it is necessary to perform the inverse Fourier transform.

2.3.2 Dipolar P^{3}M algorithm[11]

This method is based on the assignment of the dipoles on the cubic mesh sites in order to be able to apply the fast Fourier transform (FFT) in the Ewald summation procedure. Special assignment function maps particles positions in continuous space to the mesh. Then it is possible to compute reciprocal[12] and electrostatic field at each mesh point. And execute then back interpolation into the coordinate of interest. Important to note that $\breve{\phi}(\boldsymbol{k})$ from Equation 27 (what is continuum Green function) replaced by adjustable lattice Green function, so that this algorithm provides results as close as possible[13] to the results of the original continuum problem.

Two main drawbacks of FFT are truncation of the Fourier series[14] and aliasing. The dipolar energy of the interaction of a dipole with all its images in the periodic replicas of the simulation box (Madelung energy) vanishes. But in P^{3}M algorithm that is not the case, because of aforementioned disadvantages. Fortunately, this error is systematic and can be corrected. It is noteworthy that the average error for Madelung force and torque are zero.

[11] a brief description of the P^{3}M algorithm for dipolar interactions proposed in the work of Juan J. Cerdà et al. [9]

[12] optimization of the P^{3}M method affects only Equation 27, the computation of Equation 26 remains unchanged

[13] in a least-squares sense

[14] wave vectors greater than $2\pi/mesh\ spacing$ are discarded

Speaking about any algorithm, its correctness and complexity are very important. P^{3}M is not an exception. The correctness of this method can be estimated by the root-mean-square (rms) errors between the output of the algorithm (calculated dipolar forces, torques or total energy) and the exact values obtained by direct summation. There are analytical expressions for these errors that agree very well with numerical tests. Moreover, with the same set of parameters (number of mesh points, the assignment order[15], real-space cutoff and Ewald splitting parameter)[16], the errors for all three calculated values have minima located very close to each other (i.e., the correct set of parameters minimizes all three errors at once).

CPU time and scalability between presented dipolar-P^{3}M and dipolar-Ewald sum methods are presented on Figure 22.

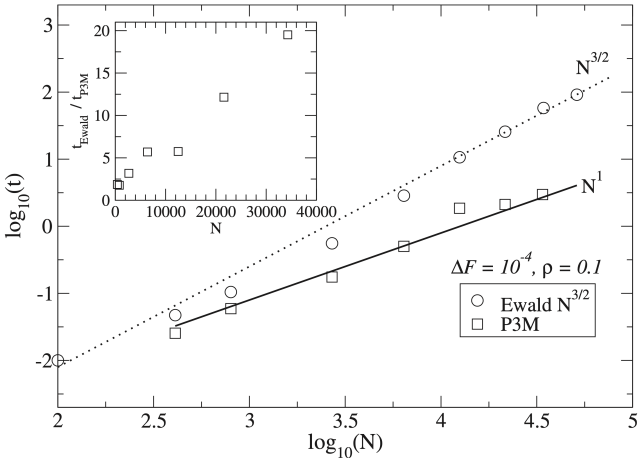

Figure 22: Time required to compute forces and torques as a function of the number of particles in the system using a typical desktop computer. The computing time t is given in seconds. Circles denote the optimal dipolar-Ewald method, and squares the new dipolar P^{3}M method. In both cases, their respective parameters have been tuned to give maximum speed at fixed force accuracy. The accuracy is set to $\Delta F = 10^{-4}$. The density of particles is $\rho = N/V = 0.1$. Lines with slopes 1 and 3/2 are plotted to guide the eye. The inset plot shows the relative speed of dipolar-P^{3}M method compared to the fastest dipolar-Ewald sum as a function of the number of particles in the system. [9].

2.4 Structure factor

The (static) structure factor is a mathematical description of probing a material with incident radiation. Based on the structural factor, computational and

[15] used in assignment function

[16] usually the first three parameters are fixed and the last one is changed to achieve the optimal error value

real results can be compared, in other words, it is a reliable bridge between simulation and reality. This section is devoted to the derivation of the structure factor equation from first principles.

2.4.1 Elastic scattering from an assembly of atoms

Assuming elastic scattering ($|\boldsymbol{k}_{in}| = |\boldsymbol{k}_{out}|$, $\boldsymbol{k}$ is a wave-vector[17]) of X-rays or neutrons (matter waves) represented as incident plane waves on sample (see Figure 23). Which then are absorbed by scattering centers (beads, MNPs) and re-emitted as spherical waves.

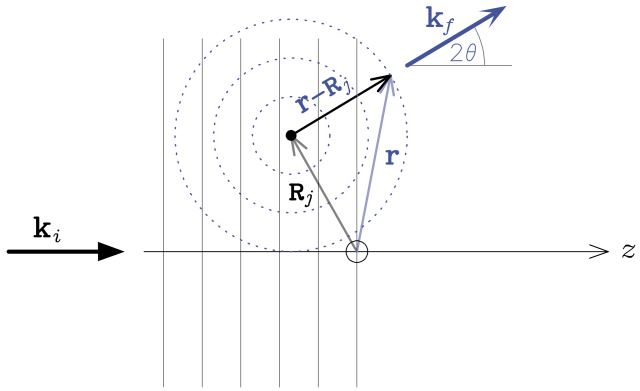

Figure 23: The contribution to the scattered wave from atom j, located at R_j relative to an arbitrarily defined origin somewhere in the sample [44].

A single re-emitted wave can be represented as:

$$[\psi_f]_j = \underbrace{\overbrace{\psi_0}^{\text{a}}\, e^{i\boldsymbol{k}_i\boldsymbol{R}_j}}_{\text{b}} \underbrace{f_j(\lambda,\theta)}_{\text{c}} \underbrace{\frac{e^{i\overbrace{\boldsymbol{k}_f}^{\text{d}}(\boldsymbol{r}-\boldsymbol{R}_j)}}{|\boldsymbol{r}-\boldsymbol{R}_j|}}_{\text{e}}. \tag{34}$$

Let us consider in detail each member of this expression:

(a) ψ_0 is the temporal variation of the wave and the phase shift[18] $\psi_0 = |\psi_0|e^{i(\phi_0-\omega t)}$;

(b) $\psi_0 e^{i\boldsymbol{k}_i\boldsymbol{R}_j}$ is a complex incident plane wave with wave-vector $\boldsymbol{k} := (0,0,k)$;

(c) $f_j(\lambda,\theta)$ is a relevant interaction characteristics of j-th particle, also referred as scattering length in neutron case and atomic form factor for the X-rays scattering. It determines scattering cross-section;

[17] its magnitude is the wavenumber $|\boldsymbol{k}| \equiv k = \frac{2\pi}{\lambda}$, where λ is the wave length

[18] usually, the phase shift is neglected, since the information "embedded in the frequencies" is enough to restore the structure of the substance

(d) $\boldsymbol{k}_f$ is a wave vector of outgoing particle;

(e) $\frac{e^{i\boldsymbol{k}_f(\boldsymbol{r}-\boldsymbol{R}_j)}}{|\boldsymbol{r}-\boldsymbol{R}_j|}$ is a re-emitted spherical wave, which decays inversely proportional to distance.

Now taking the sum over all particles, to get complete eradiation of whole sample:

$$\psi_f = \psi_0 e^{i\boldsymbol{k}_f \boldsymbol{r}} \sum_{j=1}^{N} f_j(\lambda,\theta) \frac{e^{i\overbrace{(\boldsymbol{k}_i - \boldsymbol{k}_f)}^{:=\boldsymbol{Q}}\boldsymbol{R}_j}}{|\boldsymbol{r}-\boldsymbol{R}_j|}. \tag{35}$$

Another important assumption in this model is that interference between scattered and incident beams is negligible. What is called kinematical approximation and normally holds for both X-rays and neutrons. Also only one deflection is allowed. And lastly we are taking $|\boldsymbol{r}-\boldsymbol{R}_j| = |\boldsymbol{r}| = r$ (see Figure 24).

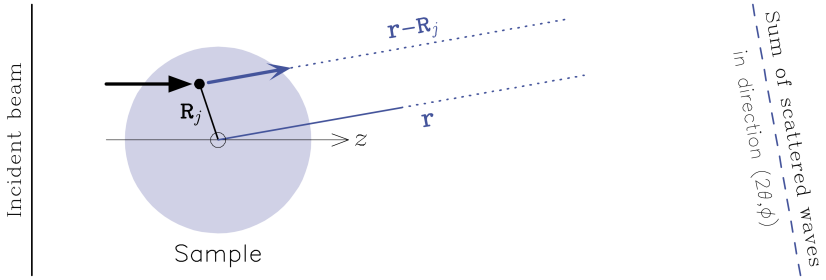

Figure 24: The size of the sample illuminated by the incident beam is usually much smaller than the distance at which scattering measurements are taken, so that $|\boldsymbol{R}_j| \ll |\boldsymbol{r}| \approx |\boldsymbol{r}-\boldsymbol{R}_j|$ for all j [44].

Finally possible to derive computationally convenient formula for structure factor, which is normalized intensity of outgoing scattering:

$$\begin{aligned} I(\boldsymbol{Q}) = |\psi_f|^2 = \psi_f \psi_f^* &= \frac{\Phi}{r^2}\left|\sum_{j=1}^{N} f_j(\lambda,\theta) e^{i\boldsymbol{Q}\boldsymbol{R}_j}\right|^2 \\ &= \frac{\Phi}{r^2}\sum_{i=1}^{N}\sum_{j=1}^{N} f_i(\lambda,\theta) f_j(\lambda,\theta) e^{i\boldsymbol{Q}\overbrace{(\boldsymbol{R}_j - \boldsymbol{R}_i)}^{:=\boldsymbol{R}_{ij}}} \\ &= [\text{if all particles are identical}] \\ &= \frac{\Phi}{r^2}\underbrace{\sum_{i=1}^{N} f_i^2(\lambda,\theta)}_{Nf^2}\sum_{i=1}^{N}\sum_{j=1}^{N} e^{i\boldsymbol{Q}\boldsymbol{R}_{ij}}. \end{aligned} \tag{36}$$

So

$$S(\boldsymbol{Q}) \equiv \frac{I(\boldsymbol{Q})}{\frac{\Phi}{r^2} N f^2} = \frac{1}{N} \sum_{i,j}^{N} e^{i\boldsymbol{Q}\boldsymbol{R}_{ij}}. \tag{37}$$

2.4.2 Debye averaging trick

Initially this idea was applied to powder of crystals. Because using this averaging on top of Laue scattering condition[19] and Ewald's sphere[20] [21] construction, one can explain radial rings in diffraction picture. Which appear instead of grid of spikes specific to bulk crystals samples.

The trick itself is to assume, that all possible mutual orientations of vectors $\boldsymbol{Q}$ and $\boldsymbol{R}_{ij}$ could be likely encountered in studied sample (what is true for the suspension of magnetic nanogels). So averaging $e^{i\boldsymbol{Q}\boldsymbol{R}_{ij}}$ means sum up $e^{i\boldsymbol{Q}\boldsymbol{R}_{ij}\cos\theta}$ for all θ and normalize by the number of different θ. What results in:

$$\left\langle e^{i\boldsymbol{Q}\boldsymbol{R}_{ij}} \right\rangle = \frac{\int_0^\pi e^{i\boldsymbol{Q}\boldsymbol{R}_{ij}} d\theta}{\int_0^\pi d\theta} = \frac{\pi J_0(|\boldsymbol{Q}||\boldsymbol{R}_{ij}|)}{\pi}, \tag{38}$$

where J_0 is zeroth order Bessel function:

$$\left\langle e^{i\boldsymbol{Q}\boldsymbol{R}_{ij}} \right\rangle = \frac{\sin QR_{ij}}{QR_{ij}}. \tag{39}$$

As a result:

$$S(Q) = \frac{1}{N} \sum_{i,j}^{N} \left\langle e^{i\boldsymbol{Q}\boldsymbol{R}_{ij}} \right\rangle = \frac{1}{N} \sum_{i,j}^{N} \frac{\sin QR_{ij}}{QR_{ij}}. \tag{40}$$

Equation 40 is computationally much more feasible[22] than Equation 37 and is used in algorithms to calculate the structure factor for systems consisting of hundreds of thousands of particles or more. Moreover, with the Debye averaging trick the resulting curve is no longer as noisy. However, it is with Equation 37 that one-dimensional (along the selected axis) or two-dimensional (in-plane) structure factor can be calculated.

[19] $\boldsymbol{k}_i - \boldsymbol{k}_f = \boldsymbol{G}$, where $\boldsymbol{G}$ is a lattice or scattering vector

[20] since scattering is elastic ($|\boldsymbol{k}_i| = |\boldsymbol{k}_f| = 2\pi/\lambda$), $\boldsymbol{G}$ must lie on the surface of a sphere (Ewald sphere) of radius $2\pi/\lambda$

[21] named after the same Paul Peter Ewald as the summation method described earlier

[22] because it is not needed anymore to rotate the $\boldsymbol{Q}$ and then average over $S(\boldsymbol{Q})$ having same $|\boldsymbol{Q}|$

2.5 Radial distribution function

The radial distribution function (RDF) $g(r)$ describes how density (number density: $\rho = N/V$) varies as a function of distance from a reference particle:

$$g(\mathbf{r}) = \frac{1}{\rho} \left\langle \sum_{i \neq 0} \delta\left(\mathbf{r} - \mathbf{r}_i\right) \right\rangle = V \frac{N-1}{N} \left\langle \delta\left(\mathbf{r} - \mathbf{r}_1\right) \right\rangle, \tag{41}$$

here $< \cdot >$ denotes the ensemble average, V is the volume of the simulation box and N is the number of particles in the system.

It is one of the most insightful tool for analyzing the structure of matter. Because on the one hand, the RDF is very easy to calculate from simulation data and interpret, and on the other hand, it is directly related to the structural factor:

$$S(\mathbf{q}) = 1 + \rho \int_V \mathrm{d}\mathbf{r} \mathrm{e}^{-i\mathbf{q}\mathbf{r}} g(\mathbf{r}). \tag{42}$$

2.6 Mean squared displacement

The mean squared displacement (MSD) is a measure of how far is the particle drifts from its starting position over time:

$$\mathrm{MSD}(t) \equiv \left\langle \left|\mathbf{x}(t) - \mathbf{x}_0\right|^2 \right\rangle = \frac{1}{N} \sum_{i=1}^{N} \left|\mathbf{x}_i(t) - \mathbf{x}_i(0)\right|^2. \tag{43}$$

One can show that $\mathrm{MSD}(t) = 2Dt$, where D is the diffusivity constant. MSD can also be measured experimentally through dynamic light scattering (for whole nanogels) or through neutron scattering.

2.7 Summary

This chapter has elucidated a magnetic nanogel model and a molecular dynamics framework. Three approaches to analyzing simulation data have been given: Structure factor, Radial distribution function and Mean squared displacement. All of them will find their application in "Results and Discussion."

The summary is a description of a simulation protocol that ties together the various sections of this chapter.

2.7.1 Simulation protocol

Suspensions were simulated by placing 100 nanogel particles obtained from the procedure described above into a periodic cubic box with a volume fraction of nanogels fixed either to 0.1 or 0.2. It is worth noting that each individual nanogel was previously equilibrated. In total, 10 different equilibrium configurations with different cross-linker and magnetic particle intrinsic distributions were used to form the suspension. This allowed us to avoid the dependence of

self-assembly on individual nanogel topology. Molecular dynamics simulations of such systems were performed with the simulation package ESPREsSo. A Langevin thermostat with fixed dimensionless temperature $T = 1$ was used to mimic the thermal fluctuations of the background fluid. The system was first equilibrated by making $2{\cdot}10^7$ integration steps, using a fixed time step $\delta t = 0.01$. subsequent measurements were obtained for 8×10^7 integration steps. Each set of parameters was sampled with 5 independent runs using different initial configurations.

Note that, in the system of dimensionless units defined above, the conventional dipolar coupling parameter, that measures the ratio between the dipole-dipole interactions and the thermal fluctuations, can be simply defined as $\lambda = \mu^2$.

Computer simulations were performed at the Vienna Scientific Cluster (VSC-3).

3 Results and Discussions

The analysis was started with the visual inspection of the equlibrated suspensions. As long as the system is rather crowded, in Figure 25(a), only the magnetic particles were shown explicitly, whereas the whole structures of each nanogel particle is represented by its convex hulls. This snapshot was obtained for $\lambda = 6$ and overall volume fraction of 0.1. In the lowest part of the snapshot (close to the centre), one can find two nanogels that seem to form a cluster. From the work where the magic microgel model was originally presented [28], it is known that inside an isolated magnetic nanogel with $\lambda = 6$, magnetic particles tend to self-assemble and form long chains close to the periphery of the nanogel to minimise the curvature. However, the translational motion required for self-assembly is often penalised by the elastic network. In case of suspension, dipolar energy can be additionally minimised if magnetic particles close to the surface of one nanogel form favourable contacts with magnetic nanoparticles of a neighbouring nanogel, thus, leading to the nanogel self-assembly, as shown in Figure 25(b).

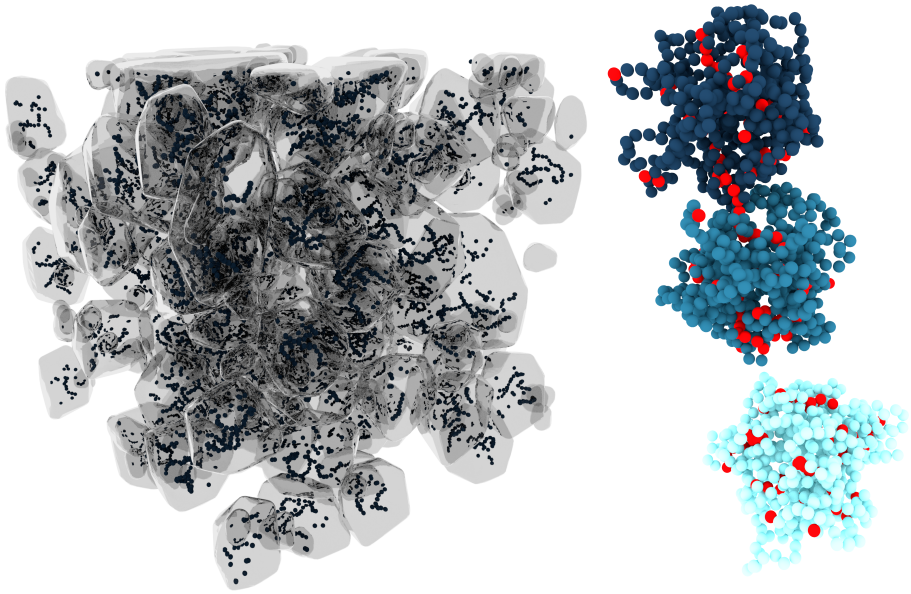

(a) (b)

Figure 25: (a) Simulation snapshot of a nanogel suspension. Volume fraction is 10 %. $\lambda = 6$. Only magnetic particles are shown explicitly, nanogels are represented by their convex hulls. (b) Zoomed in three nanogels with all beads shown explicitly. Magnetic particles are shown in red, nonnmagnetic beads of each nanogel have the same colour (light blue, blue and dark blue).

In order to understand how intensively the nanogels self-assemble, in Figures 26(a) and 26(b), radial distribution functions calculated for nanogels centres of mass was plotted. For a volume fraction of 10% (light blue curve, Figure 26(a)), one can hardly see any signature of self-assembly. The first peak of the RDF is rather small and the first minimum is not very pronounced. The situation changes for higher nanogel concentrations. Doubling the volume fraction results in a very clearly pronounced first peak at $r = 12$. It is worth mentioning here that the average nanogel radius of gyration is $R_g = 6$ and remained unchanged during the simulation ($\pm 5\%$ of the initial value). Thus, $r = 12$ corresponds to the close contact of two nanogels similar to the one shown in Figure 25(b). To exclude the possibility of having simply density fluctuation effects captured by the RDF, were also calculated the RDFs of WCA spheres suspensions with radii equal to R_g and plotted with thin red lines in Figure 26(a). The comparison between WCA spheres and actual magnetic nanogels clearly reveals the signature of self-assembly in the latter for the case 20% volume fraction: the existence of a second maximum and a deep first minimum exhibited by the RDF of nanogel suspension. Apart from concentration impact, self-assembly of magnetic nanogels can be also tuned by changing the interaction strength between MNPs. This is illustrated in Figure 26(b), where were plotted the RDFs calculated for the centres of mass of nanogels with different interaction strengths for their magnetic beads. In case of $\lambda = 4$, the RDF has a perfect shape of a noninteracting WCA-sphere liquid. In contrast, for $\lambda = 8$ the self-assembly is clearly taking place.

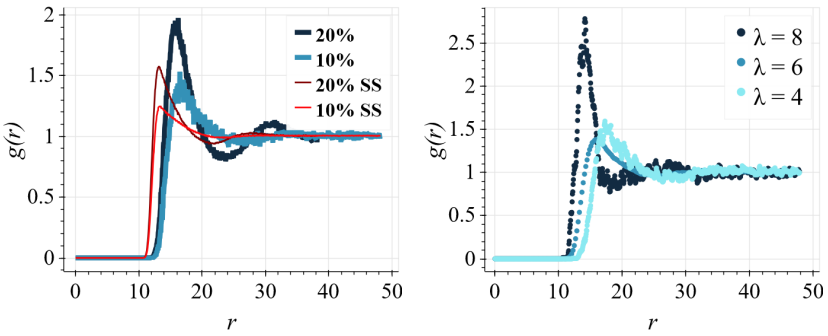

(a) (b)

Figure 26: Radial distribution functions (RDFs.) (a) and (b) – RDFs calculated for the nanogels centres of mass. Nanogels radius of gyration is on average equal to 6. (a) shows the differences in RDFs caused by changes in nanogel volume fraction; (b) shows the impact of λ on the RDFs. RDFs for equivalent suspensions of WCA spheres (SS) are also included in (a).

Further microscopic information can be revealed by calculating the RDFs corresponding only to the magnetic particles. This result is shown in Figures 27(a) and 27(b). As expected, magnetic particles in nanogels and across

them self-assemble and the tendency to form larger clusters grows with increasing nanogel concentration as well as with value of λ. Thus, for example, for $\lambda = 8$ (dark blue in Figure 27(b)), one finds well-defined peaks up to the fourth coordination shell, meaning that the chain-like magnetic structures formed in the system are rather frequent and have a significant length.

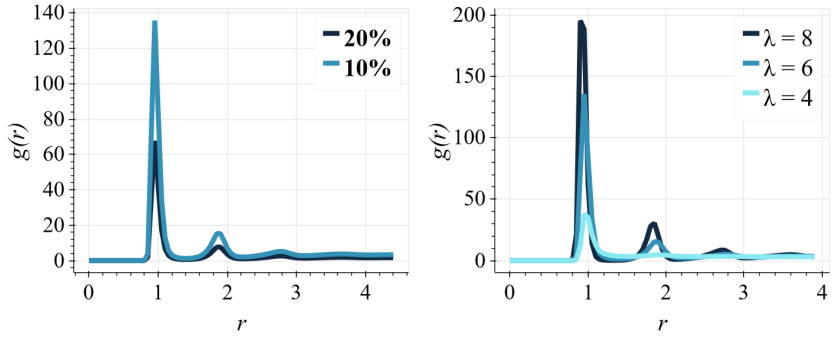

(a) (b)

Figure 27: Radial distribution functions (RDFs.) (c) and (d) – RDFs computed using exclusively magnetic particles.(c) shows the differences in RDFs caused by changes in nanogel volume fraction; (d) shows the impact of λ on the RDFs.

To answer the question whether the self-assembly of magnetic nanogels can be detected experimentally, their structure factors (SFs) were calculated. Analogously to RDFs, were computed SFs for overall nanogels and for magnetic particles only. Note these SFs, presented in Figure 29, are calculated directly from the simulation data using the Equation 37 and not as Fourier transform of the RDFs from Figure **??**.

The first peaks, $q \sim 0.5$, in Figures 28(a) and 28(b) correspond to approximately $2R_g \sim 12$ in real space. They reflect the number of nanogel pairs in close contact. Their height grows and their position shifts slightly to the right with both, increasing concentration (28(a)) and growing value of λ (28(b)). The shift of the peaks can be explained by two effects: first, the radius of gyration of magnetic nanogels decreases with λ [28]; second, when forming a contact through magnetic nanoparticles, these nanogels get deformed and can interpenetrate to a certain extent. The scale of these effects can be estimated from the shift of the SF first peak to be around 10% for $\lambda = 6$ in case of growing volume fraction, or to be around 20 % if the value of λ changes from 6 to 8 and the volume fraction is fixed to 10%.

Figure 29(a) shows the SF of magnetic nanoparticles calculated for different volume fractions and fixed $\lambda = 6$. It is clearly seen that the overall volume fraction affects only the region of small q. In fact, doubling the volume fraction of magnetic nanogels seems to not affect qualitatively the self-assembly of magnetic nanoparticles, as it was also seen in Figure 27(a). For $\lambda = 4$, the shape of SF (light blue curve, Figure 28(b)) suggests that the self-assembly is

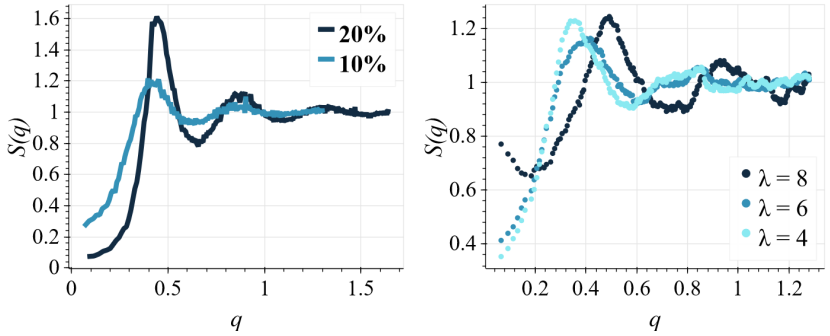

(a) (b)

Figure 28: Structure factors (SFs.) (a) and (b) – SFs calculated for whole nanogels structures. (a) shows the differences in SFs caused by changes in nanogel volume fraction; (b) shows the impact of λ on the SFs.

insignificant. This observation is confirmed by Figure 29(b), where the peak at $q \sim 7$, corresponding to the close contact of two magnetic beads, is negligible. In contrast, for $\lambda = 8$ one can clearly observe the latter peak. In Figures 29(a) and 29(b) SFs have 2 peaks for $q < 2$. In real space this corresponds to distances larger than ~ 3. Whereas the first peak at $q \sim 0.5$ is clearly related to the close contact of two nanogels at distance $2R_g \sim 12$, the second peak is more difficult to interpret. Corresponding to real distances on the order of R_g, most probably shows the correlation length of magnetic particles inside individual nanogels.

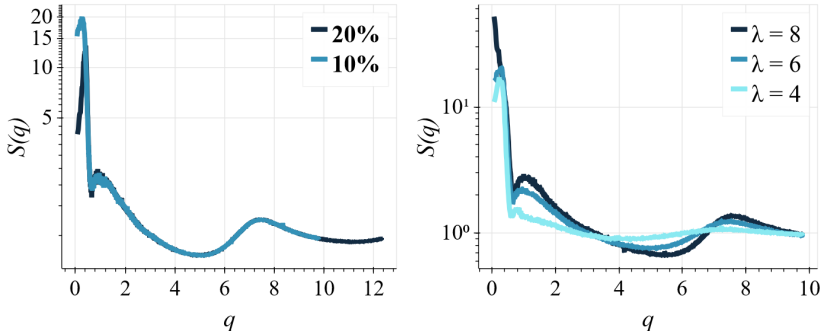

(a) (b)

Figure 29: Structure factors (SFs.) (c) and (d) – SFs computed using exclusively magnetic particles. (c) shows the differences in SFs caused by changes in nanogel volume fraction; (d) shows the impact of λ on the SFs.

Finally, having analysed all evidences of magnetic nanogel self-assembly and described the qualitative trends, in Table 1 were collected mean clusters sizes

measured for, both magnetic nanogels and individual magnetic particles, for all systems investigated here. For magnetic particles were used the distance-energy criteria of Reference [37], whereas for whole nanogels pairs were considered to be connected only if they had a shared cluster of more than three magnetic particles, with at least two of them belonging to each of the nanogels. Such a cluster parameter was chosen as an alternative to the simpler one, when two nanogels are considered to be connected if the distance between their centers of mass is less than $2R_g$ multiplied by a certain distance parameter. In the latter, the cluster sizes turn out to be very sensitive to changes in the distance parameter, which complicates further analysis (see Figure 30).

	$\lambda = 4$	$\lambda = 6$, 10 %	$\lambda = 8$	$\lambda = 6$, 20 %
MNPs	3.7	7.6	20.0	7.5
nanogels	0.2	2.1	5.2	2.6

Table 1: Cluster sizes measured for MNPs only (upper row) and for whole nanogels (lower row). For cluster definition, see the main text. The errorbars for these values are below 5 per cent.

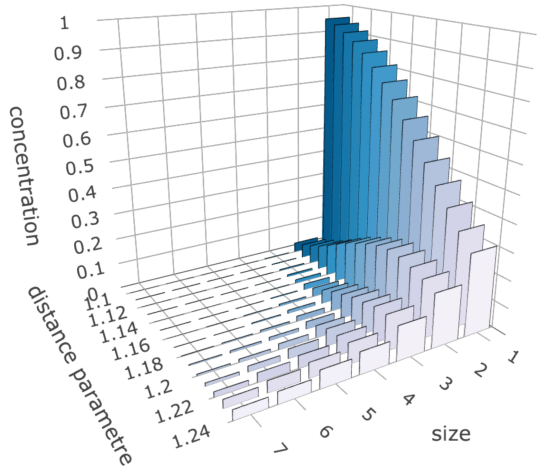

Figure 30: Normalized concentrations of clusters of different sizes of magnetic nanogels in a suspension (volume density of nanogels is 20%, $\lambda = 6$) depending on the distance parameter for simple distance based (between centers of masses) clustering criteria.

One can see that all the implicit evidences described above are fully confirmed by the cluster sizes: no aggregation is seen for magnetic nanogels for $\lambda = 4$, even though, magnetic nanoparticles do agregate; for $\lambda = 6$ was observed a moderate level of nanogel self-assembly enhanced by the increase of the volume fraction; for $\lambda = 8$ the nanogel self-assembly is very pronounced. It is worth noting here that a cluster of 5 nanogels is a relatively large object that

cannot but affect rheological and mechanical properties of these suspensions. The study of these properties is currently in progress.

It can be assumed that the average size of clusters of magnetic nanogels will noticeably affect their dynamic characteristics. This can be demonstrated by calculating the mean squared displacement of the centers of masses of the gels. For example, for $\lambda = 6$, the difference in the cluster sizes for two different volume fractions is 0.5 (this follows from the Table 1). Even such a small difference leaves an appreciable distinction on the behavior of MSD(t) in diffusion mode ($\sim t$), as it can be seen in the Figures 31(a) and 31(b). Although the behavior of this function in ballistic mode ($\sim t^2$) does not differ significantly.

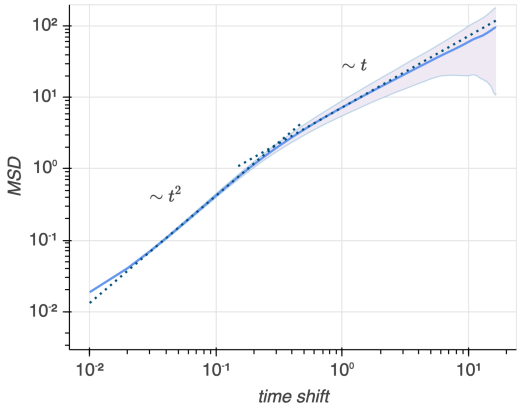

(a) 10%

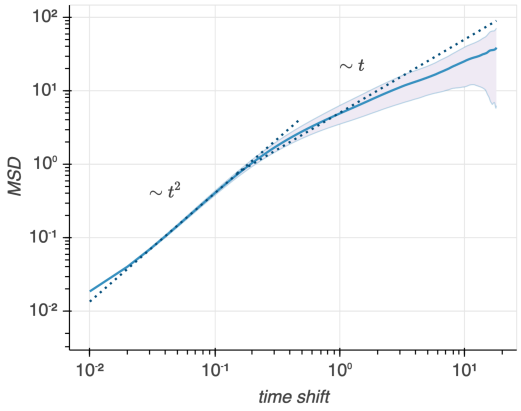

(b) 20%

Figure 31: Mean squared displacement (MSD) of centres of masses of magnetic nanogels. (a) – $\lambda = 6$, volume fraction 10% and the average cluster size is 2.1; (b) – $\lambda = 6$, volume fraction 20% and the average cluster size of magnetic nanogels is 2.6. An appreciable distinction on the behavior of MSD(t) concludes itself in the diffusion mode ($\sim t$).

4 Conclusions

In this work the influence of magnetic nanogel concentration and magnetic particle interactions on the self-assembly of magnetic nanogels in zero field was thoroughly analysed. Obtained results show that, whereas $\lambda \geq 4$ can be considered as strong self-assembly conditions for free magnetic nanoparticles, magnetic nanogels containing these particles only start forming clusters at $\lambda \geq 6$. It is worth reminding here that for individual magnetic nanogels, if the value of λ exceeds 6-7, the initial susceptibility decreases due to the fact that polymer matrix cannot hinder anymore the formation of rings of magnetic nanoparticles inside the nanogel [28]. It was found here that this effect vanished in suspensions due to the possibility of forming larger magnetic clusters with lower elastic penalty involving particles from different nanogels in close contact. These connections were shown to be responsible for nanogel self-assembly. The values of λ for which real nanogels will start forming bridges, containing magnetic particles, and self-assemble will, however, strongly depend on the crosslinking degree of the nanonogels, as the latter parameter was shown to have a nontrivial impact on the intrinsic magnetic particle self-assembly within individual nanogels [28]. The formation of bridges, albeit only qualitatively, was reported recently in Reference [54] (see, Figure 4a). The degree of clusterisation of magnetic nanoparticles inside individual nanogels, as well as between them, can be verified by scattering techniques [12, 17] as was shown by calculating magnetic nanogel structure factors. Findings of this work revealed three length-scales inherent to magnetic nanoparticles in these systems. The largest scale (region of small wave vectors q) corresponds to twice the nanogel radius of gyration and can be attributed to correlations of magnetic nanoparticles from different nanogels forming clusters; the second length-scale corresponds to the nanogel radius of gyration and may reflect the correlation length of the magnetic nanoparticles inside one nanogel; finally the smallest scale, corresponding to high values of wave vectors q, shows close contacts of nanoparticles. Heights and positions of all three SF peaks were shown to be sensitive to the value of λ. Interestingly, only the region of small q was found to depend on the nanogel volume fraction. The latter, however, plays a significant part in the amplitude of SFs if calculated for whole nanogel structures. Summarising these findings, one can expect cluster formation in suspension of magnetic nanogels, in absence of external magnetic fields, only if the interaction between embedded ferromagnetic nanoparticles is significantly higher than the values of thermal energy. However, if the self-assembly takes place, it might have a drastic effect on the structural properties even for relatively low volume fraction of the magnetic filler.

References

[1] M. P. Allen and D. J. Tildesley. *Computer Simulation of Liquids*. 2nd. USA: Oxford University Press, Inc., 2017. ISBN: 0198803206.

[2] S. Backes et al. "Loading of PNIPAM Based Microgels with CoFe2O4 Nanoparticles and Their Magnetic Response in Bulk and at Surfaces". In: *Journal of Physical Chemistry B* 119.36 (2015), pp. 12129–12137. ISSN: 15205207. DOI: 10.1021/acs.jpcb.5b03778.

[3] V. Ballenegger. "Communication: On the origin of the surface term in the Ewald formula". In: *Journal of Chemical Physics* 140.16 (2014). ISSN: 00219606. DOI: 10.1063/1.4872019. URL: http://dx.doi.org/10.1063/1.4872019.

[4] R. Barbucci et al. "A novel strategy for engineering hydrogels with ferromagnetic nanoparticles as crosslinkers of the polymer chains. Potential applications as a targeted drug delivery system". In: *Soft Matter* 7.12 (2011), pp. 5558–5565. ISSN: 1744683X. DOI: 10.1039/c1sm05174a.

[5] A. Basu et al. "Nonaffine displacements in flexible polymer networks". In: *Macromolecules* 44.6 (2011), pp. 1671–1679. ISSN: 00249297. DOI: 10.1021/ma1026803.

[6] C. Binns. "Medical applications of magnetic nanoparticles". In: *Frontiers of Nanoscience* 6 (2014), pp. 217–258. ISSN: 1876276X. DOI: 10.1016/B978-0-08-098353-0.00006-3.

[7] M. Bonini et al. "Nanomagnetic sponges for the cleaning of works of art". In: *Langmuir* 23.17 (2007), pp. 8681–8685. ISSN: 07437463. DOI: 10.1021/la701292d.

[8] N. Bou-Rabee. "Time integrators for molecular dynamics". In: *Entropy* 16.1 (2014), pp. 138–162. ISSN: 10994300. DOI: 10.3390/e16010138.

[9] J. J. Cerdà et al. "P3M algorithm for dipolar interactions". In: *Journal of Chemical Physics* 129.23 (2008). ISSN: 00219606. DOI: 10.1063/1.3000389.

[10] M. T. Cook and V. V. Khutoryanskiy. "Mucoadhesion and mucosa-mimetic materials - A mini-review". In: *International Journal of Pharmaceutics* 495.2 (2015), pp. 991–998. ISSN: 18733476. DOI: 10.1016/j.ijpharm.2015.09.064.

[11] P. Cremer et al. "A density functional approach to ferrogels This". In: *IOPscience* (2017). DOI: https://doi.org/10.1088/1361-648X/aa73bd.

[12] T. Eckert and W. Richtering. "Thermodynamic and hydrodynamic interaction in concentrated microgel suspensions: Hard or soft sphere behavior?" In: *Journal of Chemical Physics* 129.12 (2008). ISSN: 00219606. DOI: 10.1063/1.2978383.

[13] ERDEM. "Encapsulation of inorganic particles." In: *Polymeric dispersions: Principles and application* (1997), pp. 421–433. DOI: 10.1007/978-94-011-5512-0{_}28.

[14] P. P. Ewald. "Die Berechnung optischer und elektrostatischer Gitterpotentiale". In: *Annalen der Physik* 369.3 (1921), pp. 253–287. ISSN: 15213889. DOI: 10.1002/andp.19213690304.

[15] G. Filipcsei et al. "Magnetic Field-Responsive Smart Polymer Composites". In: January (2007), pp. 137–189.

[16] D. Frenkel and B. Smit. "Chapter 12 - Long-Range Interactions". In: *Understanding Molecular Simulation (Second Edition)*. Ed. by D. Frenkel and B. Smit. Second Edi. San Diego: Academic Press, 2002, pp. 291–320. ISBN: 978-0-12-267351-1. DOI: https://doi.org/10.1016/B978-012267351-1/50014-6. URL: http://www.sciencedirect.com/science/article/pii/B9780122673511500146.

[17] J. A. Galicia et al. "Local structure of polymeric ferrogels". In: *Journal of Magnetism and Magnetic Materials* 323.10 (2011), pp. 1211–1215. ISSN: 03048853. DOI: 10.1016/j.jmmm.2010.11.008. URL: http://dx.doi.org/10.1016/j.jmmm.2010.11.008.

[18] Guido Kickelbick. *Hybrid Materials: Synthesis, Characterization, and Applications*. 2007. ISBN: 9783527312993.

[19] S. A. Hollingsworth and R. O. Dror. "Molecular Dynamics Simulation for All". In: *Neuron* 99.6 (2018), pp. 1129–1143. ISSN: 10974199. DOI: 10.1016/j.neuron.2018.08.011. URL: https://doi.org/10.1016/j.neuron.2018.08.011.

[20] A. P. Hynninen and M. Dijkstra. "Phase behavior of dipolar hard and soft spheres". In: *Physical Review E - Statistical, Nonlinear, and Soft Matter Physics* 72.5 (2005), pp. 1–10. ISSN: 15393755. DOI: 10.1103/PhysRevE.72.051402.

[21] D. Ivaneyko et al. "Effects of particle distribution on mechanical properties of magneto-sensitive elastomers in a homogeneous magnetic field". In: *Condensed Matter Physics* 15.3 (2012), pp. 1–12. ISSN: 1607324X. DOI: 10.5488/CMP.15.33601.

[22] M. C. Koetting et al. "Stimulus-responsive hydrogels : Theory , modern advances , and applications". In: *Materials Science & Engineering R* 93 (2015), pp. 1–49. ISSN: 0927-796X. DOI: 10.1016/j.mser.2015.04.001. URL: http://dx.doi.org/10.1016/j.mser.2015.04.001.

[23] Q. Li et al. "Correlation between particle size/domain structure and magnetic properties of highly crystalline Fe 3 O 4 nanoparticles". In: *Scientific Reports* 7.1 (2017), pp. 1–4. ISSN: 20452322. DOI: 10.1038/s41598-017-09897-5. URL: http://dx.doi.org/10.1038/s41598-017-09897-5.

[24] B. Lu et al. "Microfluidically fabricated pH-responsive anionic amphiphilic microgels for drug release". In: *Journal of Materials Chemistry B* 4.18 (2016), pp. 3086–3093. ISSN: 2050750X. DOI: 10.1039/c5tb02378e.

[25] A. M. Mathur, S. K. Moorjani and A. B. Scranton. "Methods for Synthesis of Hydrogel Networks: A Review". In: *Journal of Macromolecular Science, Part C: Polymer Reviews* 36.2 (2007), pp. 405–430. ISSN: 1532-1797. DOI: 10.1080/15321799608015226.

[26] A. M. Menzel. "Bridging from particle to macroscopic scales in uniaxial magnetic gels". In: *Journal of Chemical Physics* 141.19 (2014). ISSN: 00219606. DOI: 10.1063/1.4901275.

[27] R. Messing et al. "Cobalt ferrite nanoparticles as multifunctional crosslinkers in PAAm ferrohydrogels". In: *Macromolecules* 44.8 (2011), pp. 2990–2999. ISSN: 00249297. DOI: 10.1021/ma102708b.

[28] E. S. Minina et al. "The influence of the magnetic filler concentration on the properties of a microgel particle: Zero-field case". In: *Journal of Magnetism and Magnetic Materials* 459 (2018), pp. 226–230. ISSN: 03048853. DOI: 10.1016/j.jmmm.2017.10.107.

[29] E. S. Minina et al. "Studying synthesis confinement effects on the internal structure of nanogels in computer simulations". In: *Journal of Molecular Liquids* 289 (2019), p. 111066. ISSN: 01677322. DOI: 10.1016/j.molliq.2019.111066. URL: https://doi.org/10.1016/j.molliq.2019.111066.

[30] N. R. Nagireddy et al. "Preparation and characterization of magnetic nanoparticles embedded in hydrogels for protein purification and metal extraction". In: *Journal of Polymer Research* 18.6 (2011), pp. 2285–2294. ISSN: 10229760. DOI: 10.1007/s10965-011-9642-2.

[31] K. Ohno, T. Nitta and H. Nakai. "SPH-based Fluid Simulation on GPU Using Verlet List and Subdivided Cell-Linked List". In: *2017 Fifth International Symposium on Computing and Networking (CANDAR)* (2017), pp. 132–138.

[32] R. Pelton and T. Hoare. *Microgels and Their Synthesis: An Introduction*. 2011, pp. 1–32. ISBN: 9783527321582. DOI: 10.1002/9783527632992.ch1.

[33] B. N. A. Peppas et al. "Hydrogels in Biology and Medicine : From Molecular Principles to Bionanotechnology **". In: (2006), pp. 1345–1360. DOI: 10.1002/adma.200501612.

[34] N. A. Peppas et al. "Hydrogels in pharmaceutical formulations". In: 50 (2000).

[35] G. Pessot et al. "Structural control of elastic moduli in ferrogels and the importance of non-affine deformations". In: *Journal of Chemical Physics* 141.12 (2014). ISSN: 00219606. DOI: 10.1063/1.4896147.

[36] E. Purcell. *Electricity and Magnetism*. 2nd ed. Cambridge University Press, 2011. DOI: 10.1017/CBO9781139005043.

[37] E. Pyanzina et al. "How to analyse the structure factor in ferrofluids with strong magnetic interactions: a combined analytic and simulation approach". In: *Mol. Phys.* 107.4–6 (2009), pp. 571–590. DOI: 10.1080/00268970902893149.

[38] B. J. Riest et al. "Coarse-Graining of Ionic Microgels : Theory and". In: 226 (2012), pp. 711–735. DOI: 10.1524/zpch.2012.0258.

[39] L. Roeder et al. "Covalent ferrohydrogels based on elongated particulate cross-linkers". In: *Macromolecules* 47.20 (2014), pp. 7200–7207. ISSN: 15205835. DOI: 10.1021/ma501396j.

[40] L. Roeder et al. "Magnetic and geometric anisotropy in particle-crosslinked ferrohydrogels". In: *Physical Chemistry Chemical Physics* 17.2 (2015), pp. 1290–1298. ISSN: 14639076. DOI: 10.1039/c4cp04493b.

[41] A. M. Rumyantsev, R. A. Gumerov and I. I. Potemkin. "Soft Matter theory vs . computer simulations". In: *Soft Matter* 12 (2016), pp. 6799–6811. ISSN: 1744-683X. DOI: 10.1039/c6sm01231k. URL: http://dx.doi.org/10.1039/c6sm01231k.

[42] H. G. Schild. "POLY (N-ISOPROPYLACRYLAMIDE): EXPERIMENT , THEORY AND APPLICATION been appearing in the literature with increasing frequency . As Fig . 1 " illustrates , growth has become rather explosive . CH3 CH3". In: 17 (1992), pp. 163–249.

[43] A. Shankar et al. "Multidomain iron nanoparticles for the preparation of polyacrylamide ferrogels". In: *Journal of Magnetism and Magnetic Materials* 431 (2017), pp. 134–137. ISSN: 03048853. DOI: 10.1016/j.jmmm.2016.08.075. URL: http://dx.doi.org/10.1016/j.jmmm.2016.08.075.

[44] D. S. Sivia. *Elementary scattering theory: For x-ray and neutron users*. 2011.

[45] Sofia S. Kantorovich et al. "Temperature-induced structural transitions in self-assembling magnetic nanocolloids". In: *PCCP* (2015). ISSN: 18426573. DOI: 10.1039/b000000x.

[46] R. F. T. Stepto et al. "Terminology of polymers and polymerization processes in dispersed systems (IUPAC Recommendations 2011)". In: *Pure and Applied Chemistry* 83.12 (2011), pp. 2229–2259. ISSN: 0033-4545. DOI: 10.1351/pac-rec-10-06-03.

[47] C. Tapeinos. *Magnetic Nanoparticles and Their Bioapplications*. Elsevier Inc., 2018, pp. 131–142. ISBN: 9780128141564. DOI: 10.1016/b978-0-12-814156-4.00009-4. URL: http://dx.doi.org/10.1016/B978-0-12-814156-4.00009-4.

[48] K. Tauer et al. "Thermal property changes of poly(N-isopropylacrylamide) microgel particles and block copolymers". In: *Colloid and Polymer Science* 287.3 (2009), pp. 299–312. ISSN: 0303402X. DOI: 10.1007/s00396-008-1984-x.

[49] S. Thaiboonrod, A. H. Milani and B. R. Saunders. "Doubly crosslinked poly(vinyl amine) microgels: Hydrogels of covalently inter-linked cationic microgel particles". In: *Journal of Materials Chemistry B* 2.1 (2014), pp. 110–119. ISSN: 20507518. DOI: 10.1039/c3tb21579b.

[50] R. Weeber et al. “Polymer architecture of magnetic gels : a review”. In: (2018).

[51] J. D. Weeks, D. Chandler and H. C. Andersen. “Role of repulsive forces in determining the equilibrium structure of simple liquids”. In: *The Journal of Chemical Physics* 54.12 (1971), pp. 5237–5247. ISSN: 00219606. DOI: 10.1063/1.1674820.

[52] F. Weik et al. “ESPResSo 4.0 – an extensible software package for simulating soft matter systems”. In: *European Physical Journal: Special Topics* 227.14 (2019), pp. 1789–1816. ISSN: 19516401. DOI: 10.1140/epjst/e2019-800186-9.

[53] Q. Wen et al. “Non-affine deformations in polymer hydrogels”. In: *Soft Matter* 8.31 (2012), pp. 8039–8049. ISSN: 17446848. DOI: 10.1039/c2sm25364j.

[54] M. U. Witt et al. “Distribution of CoFe 2 O 4 Nanoparticles Inside PNIPAM-Based Microgels of Different Cross-linker Distributions”. In: *Journal of Physical Chemistry B* 123.10 (2019), pp. 2405–2413. ISSN: 15205207. DOI: 10.1021/acs.jpcb.8b09236.

[55] J. Zhang, S. Xu and E. Kumacheva. “Polymer microgels: Reactors for semiconductor, metal, and magnetic nanoparticles”. In: *Journal of the American Chemical Society* 126.25 (2004), pp. 7908–7914. ISSN: 00027863. DOI: 10.1021/ja031523k.

[56] A. Y. Zubarev. “On the theory of the magnetic deformation of ferrogels”. In: *Soft Matter* 8.11 (2012), pp. 3174–3179. ISSN: 1744683X. DOI: 10.1039/c2sm06961j.